The DOI for this manuscript is doi: 10.1175/JPO-D-12-0117.1

The final published version of this manuscript will replace the preliminary version at the above DOI once it is available.

If you would like to cite this EOR in a separate work, please use the following full citation:

Yuan, Y., and A. Horner-Devine, 2013: Laboratory investigation of the impact of lateral spreading on buoyancy flux in a river plume. J. Phys. Oceanogr. doi:10.1175/JPO-D-12-0117.1, in press.

Laboratory investigation of the impact of lateral spreading on buoyancy flux in a river plume

Yeping Yuan * and Alexander R. Horner-Devine

Civil & Environmental Engineering, University of Washington, Seattle, WA

* *Corresponding author address:* Yeping Yuan, Civil & Environmental Engineering, 201 More Hall, Seattle, WA 98195.

E-mail: yyping@uw.edu

ABSTRACT

We investigate the relationship between lateral spreading and mixing in stratified gravity currents by comparing laterally confined and unconfined currents in a series of laboratory experiments. The vertical turbulent buoyancy flux is determined using a control volume approach with velocity and density fields derived from combined particle image velocimetry (PIV) and planar laser induced fluorescence (PLIF). Lateral spreading is determined in the unconfined experiments based on plan-view imaging using the Optical Thickness Method (OTM). We find that lateral spreading dramatically modifies the plume structure; the spreading plume layer consists of approximately linear density and velocity profiles that extend to the surface, whereas the channelized plume profiles are uniform near the surface. Lateral spreading decreases the average plume density relative to laterally confined currents with similar inflow conditions. However, the local turbulent buoyancy flux in the spreading experiments is approximately equal to that in the confined experiments. This apparent paradox is resolved when the plume areas are taken into account. The total mixing integrated over the horizontal plume area is significantly higher in the spreading experiments. Thus, the experiments suggest that spreading does not appreciably alter the turbulent mixing processes at the base of the plume. However, it significantly increases the area over which this mixing occurs and, through this mechanism, increases the net dilution of river water at a fixed distance from the river mouth. Finally, we hypothesize that the spreading does not significantly increase the local turbulent buoyancy flux because spreading occurs preferentially near the surface, whereas buoyancy flux is greatest in the core of the current.

1. Introduction

Rivers play a critical role in the exchange of material between land and the ocean. The concentration of river-borne matter and the buoyancy of river-influenced coastal waters is determined in large part by the intense mixing that occurs in the initial adjustment of the freshwater as it is discharged into the ocean. During this process outflowing buoyant river water propagates along the ocean surface and expands laterally due to the horizontal baroclinic pressure gradients. Analysis of most field observations relies on model plume propagation and mixing using theory derived from classical two-dimensional laboratory experiments, however, which do not account for the possible effects of lateral spreading. In this contribution we compare the dynamics and mixing in laboratory generated constant flux buoyant gravity currents with and without lateral spreading.

Much of our understanding of gravity current propagation is based on early lock exchange experiments, in which fluids of different densities are initially separated by a vertical barrier and then released suddenly by removing the gate. Based on potential flow theory von Karman (1940) predicted that heavy fluid with density ρ_i propagates into a semi-infinite lighter ambient fluid with density ρ_0 with a mean velocity

$$U_f = \sqrt{2g'h}, \tag{1}$$

where $g' = \frac{\Delta\rho}{\rho_0}g$ is the reduced gravity, g represents gravity, $\Delta\rho$ is the difference between the density of intrusion current and the density of the ambient water, and h is the mean current thickness behind the front. The current front is defined as the narrow region across which density changes abruptly (Garvine and Monk 1974). This was later revisited by Benjamin (1968), who arrived at the same conclusion based on energy-conserving theory for inviscid fluids. More recently Shin et al. (2004) performed experiments on surface gravity currents in a deep ambient fluid, and concluded that the Froude number $Fr = U/\sqrt{g'h}$ approaches 1 in the limit of an infinitely deep environment rather than the larger value of $\sqrt{2}$ predicted by classical work of von Karman (1940) and Benjamin (1968).

There are two effects not considered in these classical theories, which are important to the interpretation of river plumes as gravity currents. First, the lock exchange experiments involve a fixed volume of fluid, while the river inflow is fed by constant or tidally varying freshwater discharge from the estuary. Simpson (1997) showed that currents resulting from a lock release and a constant flux currents are different. For example, the frontal speed of a lock-exchange flow decreases with the depth of the active layer while a constant flux flow is independent of the depth of the active layer. Hallworth et al. (1996) concluded that the entrainment into the head of a constant flux gravity current is smaller than in the release of a fixed volume of fluid. They attributed this difference to the continual replenishment of fluid in the head by the constant feed of undiluted fluid from the tail. They compared the entrainment mechanisms and regions that entrain light fluid for constant-volume and constant-flux gravity currents. Unlike a concentrated frontal bore followed by a thin tail in the fixed volume case, the depth of the front and tail were the same in the constant flux case. Kilcher and Nash (2010) described a recent field study on the Columbia River plume and showed that varying flow rates result in significant differences in plume structure, mixing and momentum balance.

A second important difference between classical gravity current experiments and river plumes is that most prior experiments use a configuration in which the gravity currents are confined in a straight channel, whereas river plumes discharging into the ocean are laterally unconfined. A number of previous studies use axisymmetric configurations such as sector tanks to incorporate lateral effects (Britter and Simpson 1978; Chen 1980; Didden and Maxworthy 1982; Huppert and Simpson 1980; Patterson et al. 2006), noting significant structural differences in the spreading currents. For example, lateral spreading modifies the frontal propagation speed (Didden and Maxworthy 1982) and vortex stretching associated with lateral spreading gives rise to new vortical structures (Simpson 1997). Patterson et al. (2006) observed that dense fluid propagates at a relatively constant depth in channelized experiments, whereas it appears to be concentrated within the front bore in experiments with a 10 degree sector tank. These experimental results are consistent with Cantero et al. (2007), who showed that Kelvin-Helmholtz (K-H) vortices that formed at the interface in cylindrical lock release currents eventually merged to form a vortex ring near the head. The concentrated vorticity at the head of the cylindrical current initially intensifies due to vortex stretching (Patterson et al. 2006), causing the current to develop a highly turbulent front with a relatively shallow calm body (Cantero et al. 2006). An overview of the modeling of high Reynolds number gravity currents in two-dimensional and axisymmetric configurations is provided by Ungarish and Zemach (2005).

We expect that the modification of gravity current structure due to lateral spreading observed in the studies above will be relevant to the interpretation of coastal river plumes. However, the spreading dynamics observed in the previous experiments are somewhat different than river inflows because the currents were either forced to spread cylindrically or modified by the tank shape in those cases. At river mouths, the freshwater is initially channelized in the estuary and subsequently begins to spread once it reaches the coastal ocean. During this transition to the unconfined state it undergoes vertical and lateral adjustments, and the spreading rate is set dynamically based in part on the initial momentum and the density of the buoyant layer. Thus, the dynamics of unconfined gravity current generated with a constant freshwater discharge are expected to be different from both the axisymmetric and the sector tank gravity currents. To the authors' knowledge, the laboratory and numerical investigation of freely propagating gravity currents has only been reported by Rocca et al. (2008), who focused on the bottom roughness effects on three-dimensional gravity current propagation.

A number of studies have examined the detailed structure of river plumes observed in the field and made direct comparisons with prior results from gravity current experiments. Luketina and Imberger (1987) presented field observations of a tidally pulsed buoyant plume and described in detail an overturning roller at the plume front. Surface water behind the front overtook the roller and formed an energetic mixing area following the front, consistent with the previous laboratory work from Britter and Simpson (1978). Other field observations (Wright and Coleman 1971; Hetland and MacDonald 2008) suggested that the lateral spreading of buoyant plumes should behave like a lateral lock-exchange flow, which means the propagation in the alongshore direction has a similar speed as the offshore propagation in the classical lock-exchange experiment. The lateral spreading rate is proportional to the local internal gravity wave speed, c: $DW/Dt = 2c$, where W is the plume width. Since the offshore propagation speed of the buoyant layer well behind the front is initially set by the outflow momentum, this implies that the lateral spreading depends on the inflow Froude number $Fr_i = U_0/\sqrt{g_0' H_0}$, where U_0, g_0' and H_0 are inflow velocity, reduced gravity and water depth, respectively. Hetland and MacDonald (2008) and Chen et al. (2009) both suggested that lateral spreading is significantly affected by mixing in the near-field region.

Mixing due to vertical buoyancy flux through the base of the plume is commonly assumed to occur due to turbulent stratified shear layer processes (MacDonald and Geyer 2004) including Kelvin-Helmholtz (K-H) instabilities (e.g. Thorpe 1973), though mixing generated by these processes is still not well-understood (Ivey et al., 2008). Christodoulou (1986) provided an overview of turbulent mixing at the density interface through theoretical analysis and re-examination of more than 10 experimental data sets including Ellison and Turner (1959), Chu and Vanvari (1976), Buch (1980) and Pedersen (1980). He developed a general law that relates the entrainment rate ($E = w_e/U$) to the bulk Richardson number, $Ri_b = \frac{g'H}{U^2}$. Here w_e is the vertical, or entrainment, velocity through the reference isopycnal, U is the characteristic horizontal velocity, and H is the plume thickness. This analysis suggests that entrainment across the interface occurs in two different regimes. For low bulk Richardson number ($Ri_b < O(1)$), which corresponds to supercritical flow conditions, Christodoulou (1986) suggests that "vortex entrainment" occurs, in which vortices at the density interface actively distort the interface and generate turbulent mixing in the form of Kelvin-Helmholtz instabilities. In this regime, Christodoulou (1986) finds that $E \approx Ri_b^{-1/2}$. When $Ri_b > O(1)$

and the flow is subcritical, mixing is generated by the continuous bombardment of the interface by vortices generated away from the interface (Linden, 1973) as undulations in the form of Holmboe waves. This process, which is referred to as "cusp entrainment", results in a relationship with a larger exponent; $E \approx Ri_b^{-3/2}$. Both mechanisms are active in the intermediate range when Ri_b is near its critical value of unity.

Field measurements of stratified turbulence processes in plumes generally use turbulent microstructure (Nash et al., 2009) or control volume estimates (MacDonald and Geyer 2004) to determine ε, the turbulent kinetic energy dissipation rate, or $B = \frac{g}{\rho_0}\overline{\rho' w'}$, the turbulent buoyancy flux. Following from Ivey and Imberger (1991), MacDonald and Geyer (2004) used the non-dimensional variable $\frac{\varepsilon}{\Delta u g'}$ to represent the conversion of mean flow energy into turbulent kinetic energy by shear flow processes, where Δu and g' represent the shear and stratification, respectively. Subsequently, MacDonald and Chen (2012) introduced the mixing parameter $\xi = \frac{B}{\Delta u g'}$ to represent the non-dimensional turbulent buoyancy flux. Typically, B is estimated based on the control-volume method, while ε is obtained from microstructure measurements. The two can be related assuming that $P = \varepsilon + B$, where $P = -\overline{u'w'}\frac{\partial u}{\partial z}$ is the rate of turbulent kinetic energy production from the mean flow shear. This assumption is valid in homogeneous and stationary turbulence. B and P may be further related based on the assumption of constant mixing efficiency for stratified shear mixing associated with K-H billows. Ivey and Imberger (1991) suggested that K-H billows have an overturn Froude number $Fr_T = (L_o/L_t)^{2/3}$ close to unity, where $L_o = (\varepsilon/N^3)^{1/2}$ is the Ozmidov scale, L_t is the representative turbulent length scale and $N^2 = -\frac{g}{\rho_0}\frac{\partial \rho}{\partial z}$ is the buoyancy frequency. For this mechanism the mixing efficiency $R_f = \frac{B}{P} \simeq 0.2$, and thus $\varepsilon \simeq 4B$.

MacDonald and Chen (2012) investigated the relationship between spreading and mixing using a theoretical model and observations from the Merrimack River plume MA. They suggest that a quadratic relationship exists between the mixing parameter ξ and a lateral spreading parameter $\phi = \delta\frac{h}{\Delta u}$, where δ is the strain rate and h is the shear layer thickness. Their theoretical model is predicated on the idea that lateral spreading stretches individual

K-H billows that are oriented transverse to the mean flow direction, and hence increase the intensity of the billows due to conservation of angular momentum. The model predicts that the turbulent dissipation rate is proportional to the square of total plume width, thus linking turbulent mixing and plume spreading. They show that estimates of ξ and ϕ based on data from the Merrimack River plume agree with their theoretically derived relationship. The evidence from their study provides strong support for the hypothesis that spreading increases mixing. However, the conclusions from the field experiment are necessarily correlative, since it was not possible to control the spreading rate externally. The objective of the laboratory study described herein is to isolate the effect of spreading on mixing in the plume so that the relationship between the two can be clearly analyzed. We do this by conducting two identical sets of experiments, one in which the plume is confined between channel walls and is not allowed to spread, and one in which it is allowed to spread freely.

The manuscript is organized as follows. In Section 2, we describe the confined and unconfined experimental configurations and the two main measurement approaches. We present the experimental results in Section 3. In Section 4 we describe the observed relationship between spreading and mixing, and present possible hypotheses to explain the relationship. Our conclusions are summarized in Section 6.

2. Experimental Set-up

A schematic of the laboratory set-up is shown in Figure 1. All experiments were conducted in a water tank (hereafter called the plume basin), which is 400 cm long, 250 cm wide and 50 cm deep. The buoyant water source was a 600 l constant head tank located 5 m above the level of the plume basin. The inflow was introduced into the plume basin through a small estuary tank, containing a diffuser board and a honeycomb to achieve uniform flow and a 30 cm (W_0) $\times$ 5 cm (H_0) channel section. The origin of the Cartesian coordinate is defined at the center of the river mouth water surface, x is the onshore coordinate, y is the alongshore coordinate, and z is the vertical coordinate with positive upward. The coordinate system and the plume basin dimensions are shown in the schematics in Figure 1. Each experiment started by opening the estuary gate and the buoyant water valve simultaneously. After propagating across the plume basin, mixed fluid exited the system over an adjustable weir at the downstream end of the basin.

Two configurations were designed with different estuary tank locations to determine how lateral spreading affects plume structure. In the unconfined case the estuary tank was located at the center of one end of the plume basin (Figure 1a). By lifting the gate and opening the valve, the buoyant fluid was released from the estuary channel into the ambient water where it was allowed to spread freely. For the confined case the estuary tank was oriented between the tank wall and a vertical plastic wall so that these formed transparent lateral boundaries (Figure 1b). The current stayed within the channel as in the classical lock-exchange experiment, but received a constant flux of buoyant fluid.

a. Plume structure and width measurements

For visualization purposes, the freshwater was dyed with colored food dye and the plume freshwater thickness field was measured using the optical thickness method (OTM) (Cenedese and Dalziel 1998; Yuan et al. 2011). The food dye was added in the source water and illuminated by a point light source located above the plume basin. A sequence of images were acquired with a digital camera mounted perpendicular to the water surface. We describe the plume based on the freshwater thickness h_e, which is calculated according to:

$$\frac{I(h_e, C_0)}{I_0(h_e, 0)} = e^{-\theta C_0 h_e}, \tag{2}$$

where $I(h_e, C_0)$ is the transmitted intensity of light passing through a distance h_e of fluid with dye concentration C_0. The attenuation coefficient θ is determined using a calibration with a wedge-shape cuvette before each experiment. The effects of absorbed light by the tank bottom, as well as the non-uniformity of the background light from a single point source are minimized by normalizing the intensity of dyed water to the transmitted intensity for the same thickness of undyed water, $I_0(h_e, 0)$, at each pixel.

Note that h_e is the 'effective' freshwater thickness, which is equivalent to the unmixed plume layer thickness (Yuan et al. 2011). The real thickness of dyed water in the plume is always larger than the effective freshwater thickness we measured, as the plume is continually diluted by entraining undyed ambient salt water. However, these experiments, which we refer to as the plan-view experiments (Figure 1c), provided comprehensive imaging of the entire plume structure that compliments the detailed quantitative velocity and density measurements described in §2.b. The data from the plan-view experiments are used to determine the plume width and spreading rate.

b. Velocity and density measurements

We investigated the detailed interfacial dynamics and mixing processes in the plume (Figure 1d) using a combined particle image velocimetry (PIV) and planar laser induced fluorescence (PLIF) technique developed by Cowen et al. (2001). A description of this method and its implementation for stratified flows using a similar set-up are given by Horner-Devine (2006). This technique measures velocity and density fields at short time intervals from a sequence of image triplets taken with a digital camera fitted with a wavelength cut-off filter. It requires laser sheets from both ND:YAG laser (Solo 200XT, New Wave Laser) and Argon ion laser (Innova 306, Coherent) located beside the plume basin. The laser beams are directed horizontally beneath the plume basin and steered vertically through a cylindrical lens to produce vertical laser sheets that are located on the plume axis and are carefully aligned in the offshore direction. A 1024 by 1024 pixel CCD camera (Dalsa Coorperation) is positioned 1 m from the plume centerline, and provides images in the vertical - offshore plane of the plume with a 12 cm by 14 cm field of view. The velocity field is obtained from the first two images within one triplet sequence. These images are illuminated by the ND:YAG laser, which has a wavelength higher than the cut-off wavelength so that the light scattered from the particles can pass the filter. The images are processed to generate velocity fields using matPIV (Sveen 2004). The third image in the sequence is illuminated by the Argon ion laser and processed using the PLIF technique (Crimaldi 2008). The PLIF concentration images are converted to density using a MicroScale Conductivity and Temperature Instrument (MSCTI, PME Inc.) probe located at the outer edge of laser field. The probe was mounted to a vertical profiler generated by a step motor and controlled by an Adruino board.

Ten plan-view experiments were conducted in the spreading configuration prior to the quantitative PIV-PLIF experiment. Sixteen runs with PIV-PLIF method were conducted in total, with eight in the channelized configuration and eight in the spreading configuration. Each set of channelized and spreading experiments were designed to have similar inflow conditions (similar Fr_i). The inflow condition was controlled by the inflow flow rate Q_0 and inflow reduced gravity $g_0' = \frac{\rho_0 - \rho_i}{\rho_0} g$, where ρ_0 is the ambient water density and ρ_i is the inflow water density. However, due to experimental limitations, it was impossible to match g_0' exactly. Experimental parameters for all runs are provided in Table 1. The inflow Froude number (Fr_i) ranged from 0.25 to 2.14, including subcritical and supercritical conditions. The inflow Reynolds number ($Re = \frac{\rho_i U_0 H_0}{\mu}$) are listed in the last column, where ρ_i, U_0 and H_0 are the inflow density, velocity and water height, μ is the dynamic viscosity of the water.

3. Results

a. General Plume Description

The development of a freely spreading gravity current is shown in the first row of Figures 2 (a-c) and 3 (a-c), which show freshwater thickness fields of the flow. Corresponding vertical density fields overlain with simultaneous velocity profiles from the vertical PIV-PLIF measurement are shown below the plan-view images (Figures 2d-f and 3d-f). For comparison, vertical density fields and velocity profiles for confined cases with similar inflow conditions are plotted in the third row in Figures 2 (g-i) and 3 (g-i) at the same time.

In the unconfined case the inflowing buoyant water is observed to spread laterally and form a cone-shaped surface layer. The structure and evolution of this surface layer depends on the inflow Froude number. In the high inflow Froude number run (PL4: $Fr_i = 1.68$), the flow is supercritical and the plume consists of a jet-like current with an offshore velocity higher than the alongshore velocity (Figure 2a-c). In the low inflow Froude number case (PL6: $Fr_i = 0.50$) the flow is subcritical and the plume shape is semi-circular (Figure 3a-c).

There are several points worth noting regarding lateral spreading. First, although the plume shoals significantly in unconfined cases, the frontal bore has a thickness similar to the confined case. The frontal bore is a cavity filled with the lighter fluid, which has the sharp density gradient at the leading edge and the enhanced turbulence at the lee side. This structure is similar to the laboratory observations of lock-exchange experiment (Patterson et al. 2006; Simpson 1997) and to the field observation of small buoyant plumes (Luketina and Imberger 1987; Garvine and Monk 1974). The thick layer in the frontal bore appears as a slightly brighter band, relative to the region immediately inside of it, pointed by the leftmost solid arrow in the freshwater thickness field (Figures 2a-b and 3a-b). In the high Fr_i confined case (Figure 2i), we observe an approximately 6 cm thick frontal bore and a constant thickness (approximately 4 cm) trailing current behind it. In contrast, in the high Fr_i unconfined case (Figure 2f) an approximately 6 cm deep frontal bore is followed by less than 2 cm layer (not shown in the figure). This phenomenon is consistent with observations in previous laboratory studies (Patterson et al. 2006) and numerical simulations (Cantero et al. 2007) on cylindrical spreading gravity currents.

In the unconfined cases the density field shows a clear shear-induced vortex billow in the frontal bore (Figures 2e and 3e), which is generated by Kelvin-Helmholtz instability at the interface. The instability is more developed in the unconfined case than the confined case, where the billows are not as distinct. After the front has passed, the interface is continually deformed with a similar structure. On the leading edge of each wave the interface becomes very sharp and the buoyant layer thickens (Figures 2f and 3f). The trailing edge is marked by intense mixing as the buoyant layer thins again, often nearly to zero thickness. This periodic oscillation of the plume thickness is also observed in the plan-view freshwater thickness field as deep bands near the river mouth. This structure, together with the frontal bore structure discussed in the previous paragraph, is marked with arrows in the plan-view freshwater thickness field (Figures 2c and 3c). Although both structures are clearly observed in the freshwater thickness video, they are a little hard to be identified in still images.

In contrast, mixing in the confined current occurs within a fairly uniform mixing layer at the interface (Figures 2i and 3i). The interface is more diffuse and the scale of the interface excursions in the mixing region is significantly smaller than in the unconfined case. In particular, there is no evidence of the low-wavenumber interface oscillation structures along the interface. The cause of these structures and their relationship to plume spreading will be investigated in future work.

The velocity profiles in Figures 2 and 3 are the instantaneous front-relative offshore velocity, generated by subtracting the frontal propagation speed, u_f. The frontal propagation speed is calculated based on a linear fit of front position (x_f) versus time (t). Negative velocities imply that the velocity in the buoyant layer exceeds the frontal propagation speed (i.e., $u > u_f$). These results clearly show that fluid in the plume body is overtaking the plume front (Figures 2e, h and 3e, h). The maximum velocity of the fluid within the plume front and body was typically around 40% to 60% faster than the frontal propagation speed in our experiments. This result is in agreement with earlier numerical simulations (Hartel et al. 2000) and laboratory observations (Thomas et al. 2003) of a two-dimensional gravity current, which find that velocities just behind the gravity current head were typically 20% higher than the frontal velocity. The axisymmetric gravity current was reported to have velocities in the tail up to 40% of that of the front (Patterson et al. 2006).

b. *Plume Width and Global Spreading Rate*

After sufficient time, the plume is considered to be in a steady state because the flow rate of plume water leaving the basin over the weir matches the inflow discharge. This was confirmed based on the vertical velocity and density fields. The mean plume freshwater thickness, which is based on an average over 100 seconds (500 images), is highest near the plume center and decreases both in the offshore and in the alongshore direction (Figure 4a). The freshwater thickness contours in the high Fr_i run are half ellipses with major semi-axes located at the plume centerline. The freshwater thickness contours in the low Fr_i run are approximately semi-circles (not shown).

As discussed in §2, the freshwater thickness h_e is equivalent to the layer thickness in the absence of mixing. It has no dynamical meaning; however, it is valuable for estimating the plume width and the lateral spreading rate since it represents the total amount of freshwater at each point. A centered non-normalized Gaussian fit was successful in describing the lateral distribution of h_e at each location along the plume axis (Figure 4b). We define the plume width in terms of the variance of the Gaussian fit $b = C\sigma$. For the present experiments the coefficient C is set to be 4 for two reasons. First, it is observed to account for most of the cross-sectional area in the Gaussian distribution. Second, this value fits the freshwater conservation (the detailed calculation will be discussed in §3.e). Moving offshore, h_e decreases exponentially (Figure 4c) and the width increases exponentially (Figure 4d). The plume width exponential fit is referenced to a virtual origin at $x = x_0$, which is different for each experiment, but constant within each experiment after the plume reaches steady-state. The corrected offshore distance, r, is defined as the distance from the virtual origin $r = x - x_0$. Note that this is different from the virtual origin used to describe frontal propagation (Luketina and Imberger 1987; Kilcher and Nash 2010). In the case of the front, the virtual origin is defined as the origin of a circular fit to the plume front, which typically moves offshore at a constant speed. In the present experiment, the plume is modeled as expanding radially and so the terminology is consistent with this model.

Hetland and MacDonald (2008) defined the global spreading rate as $\alpha = \frac{\Delta r/r}{\Delta b/b}$, which relates the relative change in width to the relative change in radial distance. The radial distance is the same as the corrected offshore distance in the present experiment. They use this parameter to differentiate between divergent plumes ($\alpha < 1$), in which the lateral expansion of the flow is faster than the offshore propagation, and convergent plumes ($\alpha > 1$) in which the lateral expansion is slower than the offshore propagation. We determine the spreading rate by fitting an exponential curve $\sigma = a(x - x_0)^n$ to the width (recall that $b = 4 \times \sigma$) profile for every case. A simple derivation shows that the global spreading rate, α, is the reciprocal of the exponent n:

$$\frac{db}{b} = n\frac{d(x - x_0)}{x - x_0} = \frac{1}{\alpha}\frac{dr}{r}. \tag{3}$$

The spreading rate α decreases with increasing Fr_i (Figure 5), indicating a shift toward divergent plumes (e.g. Figure 2a-c) for higher Fr_i. A divergent plume is more like an energetic jet, the lateral expansion of the flow is faster than the movement of that parcel away from the source as illustrated in Figure 2b and 2c. A divergent plume has streamlines that are more splayed than they would be with uniform radial spreading. Lower Fr_i has a higher spreading rate α, the plume will spread laterally more slowly as it flows away from the estuary mouth (Figure 3a-c). In the convergent plume case inflow momentum is less important, radial and lateral spreading are balanced, and the depth contours are circular. It is important to note that the inflow parameter in plan-view experiments and PIV-PLIF experiments are not perfectly matched. The spreading rate α of three spreading runs, which do not have plan-view freshwater thickness field, was extrapolated from Figure 5 and then was used to calculate the plume width in the control-volume method (§3.e).

c. *Density and Velocity Profiles*

In Figure 6 the average plume density and velocity profiles are plotted for all sixteen runs with different inflow Froude numbers. The profiles are averaged in time over 500 seconds during the steady state period and in the offshore direction over the PIV/PLIF field of view. The vertical axis is normalized by the plume thickness, H_p, which is defined as the depth of the 95% total freshwater flux contour. Here, the freshwater flux is calculated from the density and velocity field according to $Q_f(x,z) = \int_z^0 \frac{\rho_0-\rho(x,z)}{\rho_0-\rho_i} u(x,z)dz$, where u, ρ are the time averaged velocity and density along plume centerline ($y=0$) over 500s, and hence Q_f is the flux per unit width along the centerline.

Density and the velocity profiles are noticeably different in the channelized and spreading cases. In all of the channelized runs, both density and velocity profiles exhibit a step-wise structure consisting of a mixing layer, where the profiles vary nearly linearly, in between a near-surface uniform density layer and the underlying quiescent ambient water. This structure is similar to the density and velocity profiles in channelized gravity current laboratory experiments (Britter and Simpson 1978; Didden and Maxworthy 1982) and in the two-layer flow in salt-wedge estuary channels (MacDonald and Horner-Devine 2008; Tedford et al. 2009a). The near-surface uniform density layer disappears in the spreading cases; velocity increases (density decreases) approximately linearly all the way to the water surface. This structure is consistent with field observations from river plumes, including the Columbia (Kilcher et al. 2012), Fraser (MacDonald and Geyer 2004), and Merrimack (MacDonald et al. 2007) river plumes.

Profiles from two low Froude number spreading runs (SP5 and SP6, Table 1) have slightly different structures from the rest of the runs. Firstly, the interface thickness for velocity profile is much greater. Secondly, the center of the interface is offset downward in the velocity profile compared with the density profile. Thorpe (1971) suggested that the co-location of the density gradient and velocity shear is essential for generating K-H instabilities. Lawrence et al. (1991) showed that Holmboe instabilities can occur when the shear interface thickness is larger than the density interface and the inflection points of the two profiles are displaced. This suggests that these two runs may be susceptible to Holmboe instabilities. Instabilities observed at the interface for run SP5 (Figure 3f) have a similar character to the Holmboe instabilities observed in exchange flow laboratory experiments by Tedford et al. (2009b). These low Fr_i instabilities may indicate that the plume is in a slightly different mixing regime for these two runs. In particular, these runs may exhibit cusp entrainment as opposed to vortex entrainment as described by Christodoulou (1986).

d. Plume density

The average density of the plume layer at a point sufficiently far from the river mouth determines the buoyancy available to drive far field plume processes such as alongshore penetration and freshwater flux, and is related to the net dilution of river-borne matter. The average density at this point is a consequence of the mixing and advection processes in the near-field region. Here we compare the average plume density at the offshore end of our measurement region to see if there is a difference between spreading and channelized plumes. We define the buoyancy anomaly β as:

$$\beta = \frac{\Delta\rho_0}{\Delta\rho} = \frac{\rho_0 - \rho_i}{\rho_0 - \rho_p}, \tag{4}$$

where $\rho_p = \frac{1}{H_p}\int_{-H_p}^{0} \rho(z)dz$ is the plume density averaged vertically over the entire plume layer at plume centerline. The buoyancy anomaly β is the reciprocal of the normalized density anomaly, $\frac{\Delta\rho}{\Delta\rho_0}$, which quantifies the net mixing (or, plume dilution) that has occurred between the river mouth and the measurement location (Hetland 2010). Larger values of β indicate a higher average plume density at the measurement location, thus more mixing has occurred. The relationship between β and Fr_i is shown in Figure 7. Errors are estimated based on the standard deviation of the average plume density. The average error for all spreading and channelized cases are shown separately in Figure 7. We observe that β is higher in the spreading cases than the channelized cases: the average value of β in the channelized cases is 2.8 ± 0.4, while in the spreading cases is 3.7 ± 0.6. Note however that three points, highlighted by cross symbols in Figure 7, have opposite result. Two low Fr_i spreading runs (SP5 and SP6) have extremely low value of β. These may be because they are in a different mixing regime as we discussed in the previous section. The measurement error associated with low Fr_i spreading runs is also higher than the other runs because of the limited amount of usable data in PIV measurements. The anomalous result of the low Fr_i channelized run (CH1) is unclear. The buoyancy anomaly β shows little dependence on Fr_i in the channelized cases over the parameter range of these experiments.

We expect that the buoyancy anomaly observed in the channelized runs is strongly influenced by the near-surface uniform density layer, which is not actively mixing due to the lack of density gradient but is included in the calculation of the average density anomaly. We investigate whether the difference in β between the spreading and channelized runs may be attributed to the disappearance of this surface layer in the spreading cases, rather than differences in the intensity of mixing processes at the interface. In order to test this we limit the averaging in ρ_p to include only the mixing layer. The plume buoyancy anomaly with only the mixing layer β_{ML} is the same in the spreading (3.7 ± 0.6) and channelized (3.7 ± 0.9) runs, within the experimental errors. Thus, the modification of the density in the mixing layers is the same in both cases, suggesting that the intensity of mixing is the same. This result suggests that the differences observed in the buoyancy anomaly β (Figure 7), must be due to advection processes rather than mixing. Differences in mixing will be quantified in terms of the entrainment rate and buoyancy flux in §3.e and §3.f.

Based on a simple theoretical model, Hetland (2010) predicts that the normalized density anomaly anomaly ($1/\beta$) at the end of near-field plume is a function of $w_e b_0^2/Q_{f0}$, where w_e is the entrainment velocity, and b_0 and Q_{f0} are the inflow width and freshwater flow rate, respectively. The field of view in our experiment is close to the end of the near-field region, though it is likely to be somewhat inside the near-field due to constraints in the experimental set-up. The buoyancy anomaly at this point may provide insight into how $\Delta\rho$ changes with inflow conditions and lateral boundary conditions. In the Hetland (2010) model, increasing freshwater inflow results in a decreasing normalized density anomaly at the end of near field region. The decrease in the normalized density anomaly, which appears as an increase in β, with Fr_i observed in the spreading cases (Figure 7 black dash line) is consistent with this prediction. Leaving out two anomalous points (SP5 and SP6), we still observe an increase in β with Fr_i (Figure 7 shaded dash line) in spreading runs but with a significant smaller slope. On the other hand, the tendency of β on Fr_i in the channelized runs (Figure 7 black and shaded solid lines) are opposite with and without the anomalous run (CH1). However, both slopes are small compared to spreading ones thus we conclude that no clear relationship is observed between β and Fr_i in the channelized runs.

e. Total Vertical Density Flux and Entrainment Velocity

A direct measurement of the bulk entrainment into the freshwater plume is obtained by calculating the total vertical density flux through the plume base using a control volume approach (MacDonald and Geyer 2004). This technique has been successfully applied for measuring buoyancy, momentum and sediment fluxes in the Merrimack (MacDonald et al. 2007) and Columbia (Kilcher et al. 2012; Nowacki et al. 2012) river plume. MacDonald et al. (2007) confirmed that the control volume results have an excellent agreement with the Regional Ocean Modeling system (ROMS) numerical model output, and are consistent with direct measurement of turbulent dissipation by autonomous underwater vehicle (AUV) microstructure. The method involves conservation of volume and mass within a control volume (CV) bounded by the following control surfaces (CS): river mouth, end of the field of view, two lateral boundaries, water surface and a specified bottom isopycnal. Conservation of volume and mass are expressed according to

$$\iint\limits_{CS} \vec{U} \cdot d\vec{A} = \frac{\partial}{\partial t}\left[\iiint\limits_{CV} dV\right]; \tag{5}$$

$$\iint\limits_{CS} \rho\vec{U} \cdot d\vec{A} = \frac{\partial}{\partial t}\left[\iiint\limits_{CV} \rho dV\right]. \tag{6}$$

The right hand side of both equations reduces to zero once the plume layer reaches the steady state. We assume that there is no flux through the water surface and two lateral boundaries, i.e., almost all mixing occurs at the plume base. With these simplifications, equations 5 and 6 equate diapycnal volume and density fluxes with vertically integrated offshore volume and density fluxes above a specified isopycnal:

$$\int_z^0 \int_{-b/2}^{b/2} udydz|_{x=0}^{x=x} - \int_0^x \int_{-b/2}^{b/2} wdydx = 0; \tag{7}$$

$$\int_z^0 \int_{-b/2}^{b/2} \rho udydz|_{x=0}^{x=x} - \int_0^x \int_{-b/2}^{b/2} \rho wdydx = 0. \tag{8}$$

Horizontal volume and density fluxes along the plume centerline are calculated from the time averaged density (ρ) and offshore velocity (u) profiles shown in Figure 6. The velocity and density fields are then assumed to be laterally uniform and the integral in the y direction is accounted for by multiplying by the width, b. There are two different ways to estimate the plume width. One is from the freshwater conservation in the control-volume analysis in MacDonald and Geyer (2004): $Q_{f0} = b(x)\int_{-H}^0 \frac{\rho_0-\rho(x,z)}{\rho_0-\rho_i}u(x,z)dz$, where H is the total water depth. The other way to compute the plume width is from the plan-view experiment (i.e. $b = 4 \times \sigma$) as shown in §3.b. For our experiments, the value of b computed using freshwater conservation agreed well with the value from plan-view experiments method, and the latter definition was used in the calculations because it was less noisy. It is important to note, however, the way to calculate b accounts to some extent for non-uniformity in u and ρ because of the conservation of freshwater. Equations 7 and 8 can then be re-expressed in terms of the laterally averaged diapycnal velocity $\bar{w}$ and density flux $Q_v = \frac{g}{\rho_0}\overline{\rho w}$ through each isopycnal,

$$\frac{\partial}{\partial x}\left[\int_z^0 budz\right] - \overline{w}b = 0; \tag{9}$$

$$\frac{\partial}{\partial x}\left[\int_z^0 \rho budz\right] - \overline{\rho w}b = 0. \tag{10}$$

Finally, the Reynolds salt flux is determined according to $\overline{\rho' w'} = \overline{\rho w} - \bar{\rho}\bar{w}$. The vertical advective density flux $\bar{\rho}\bar{w}$ is calculated by multiplying the diapycnal velocity determined from equation 9 with the density of the bounding isopycnal. Profiles of $\bar{w}$ show that it is negative at the surface and positive below the plume base (Figure 8a, c). This is consistent with the entrainment velocity profile from the Fraser River plume lift-off (MacDonald and Geyer 2004), indicating a developing mixing layer that is entraining fluid from both the surface and deep water.

Channelized and spreading cases both show similar structure in the total vertical density flux and entrainment velocity profiles (Figure 8). Note that in the channelized cases the maximum positive and the maximum negative entrainment velocity are almost the same, while in the spreading cases the maximum positive entrainment velocity from below is larger than the maximum negative entrainment velocity at the surface. This is because there is a distinct, uniform upper layer in the channelized case from which the buoyant fluid can be entrained down to the mixing layer. In the spreading case, however, there is no such freshwater source at the surface so the entrainment into the mixing layer from above (negative $\bar{w}$) is smaller than from below (positive $\bar{w}$).

For comparison with previous experiments we compute the entrainment rate, defined as $E = w_e/U$, where w_e is the maximum vertical velocity through the lowest isopycnal (i.e., the maximum value of $\bar{w}$ in the profile) and U is the layer-averaged velocity in the plume. Morton et al. (1956) first developed the idea of an entrainment rate to quantify the flow of ambient fluid into the turbulent layer. Ellison and Turner (1959) carried out surface jet experiments in a long, narrow, rectangular channel, similar to our channelized configurations. They calculated E based on conservation of volume and related it to the local bulk Richardson number Ri_b. They concluded that E decays exponentially according to Ri_b^{γ} and that entrainment becomes negligible for $Ri_b > 0.8$ in the surface jet. Christodoulou (1986) summarized all available experimental results for a variety of flow types and proposed governing laws for the dependence of the E on Ri_b. He found that $\gamma \approx -1/2$ at small Ri_b and progressively increases to $-3/2$ for large Ri_b in buoyant overflows.

We calculate the local bulk Richardson number using $Ri_b = \frac{g'_m H_p}{U_m^2}$, where g'_m is the maximum reduced gravity corresponding to the maximum density anomaly $(\rho_0 - \rho_{min})$ and U_m is the maximum streamwise velocity within the plume layer. The entrainment rate E from the present experiments is plotted against bulk Richardson number in Figure 9a, along with those of Ellison and Turner (1959); Chu and Vanvari (1976); Pedersen (1980); Buch (1980), as summarized by Christodoulou (1986). Our data are in the low Ri_b regime and are in good agreement with data from Ellison and Turner (1959) in a similar Ri_b range. Two low Fr_i runs have significantly lower entrainment rates (diamonds in Figure 9a inset). These correspond to very thin buoyant layers and we hypothesize that they may be in a different regime than the other runs as described previously. Excluding those two points, data from the present experiments follow a $E = k_1 Ri_b^{-1/2}$ relationship in the region of $Ri_b < O(1)$, where in the present experiment $k_1 = 0.02$. This Ri_b region is described by Christodoulou (1986) as the region where the mixing takes place through vortex entrainment.

It is also valuable to investigate the dependence of E on Fr_i, which is an independent parameter describing the strength of the inflow as opposed to Ri_b which characterizes the sheared flow observed in situ. We observe a clear linear relationship between E and Fr_i for all experiments (Figure 9b). The data shows no significant difference in entrainment rate between spreading and channelized cases, suggesting again that local mixing is not modified by lateral spreading. Entrainment parameterizations based on the bulk Richardson number such as Ellison and Turner (1959) require a priori knowledge of the current properties, which makes the analytical theory complex or even unsolvable (Hetland 2010). Simpler parameterizations, such as $E =$ constant or $w_e =$ constant have also been commonly used in numerical modeling, but do not capture the dependence of mixing on inflow conditions. Our result indicates a simple relation between the entrainment rate and inflow Froude number, $E = aFr_i$. This suggests Fr_i controls the total energy input to the plume system, and highlights the usefulness of using Fr_i to predict the amount of entrainment and mixing in the near field plume region.

Moreover, the relationship between Froude number and the bulk Richardson number ($Ri_b = 1/Fr^2$) shows that the inflow bulk Richardson number (here we call it Ri_{bi}) also fits the relationship suggested by Christodoulou (1986): $E = k_2 Ri_{bi}^{-1/2}$, where $k_2 = 0.03$. Although both in-situ and inflow Richardson numbers agree with the empirical relationship between entrainment rate and Richardson number, the in-situ measurement shows more scatter and weaker fit. Note that there are errors in measuring the density and velocity field and calculating the plume thickness (H_p) and hence Ri_b in the plume layer, which may explain some of the difference. More importantly, however, the in-situ calculation of Ri_b uses the velocity and density at the end of the field of view, while most of the mixing happens near the lift-off region. The inflow Richardson number (or Froude number) describes the initial conditions at the inflow and may represent the potential for mixing. This appears to be a better way to predict the actual amount of entrainment.

f. Turbulent buoyancy flux

The turbulent buoyancy flux is a direct measure of mixing due to turbulence that can be estimated from the available data using the control volume method (MacDonald and Geyer 2004). It is defined as:

$$B = \frac{g}{\rho_0}\overline{\rho' w'} = \frac{g}{\rho_0}\left(\overline{\rho w} - \bar{\rho}\bar{w}\right). \tag{11}$$

where $\frac{g}{\rho_0}\overline{\rho w}$ and $\frac{g}{\rho_0}\bar{\rho}\bar{w}$ are the total and mean vertical density fluxes through isohalines, respectively. The mean flux is the same order of magnitude as the total and the turbulent buoyancy flux is approximately two orders of magnitude smaller. In all cases, the shapes of the turbulent buoyancy flux profiles are relatively similar (Figure 10). The peak buoyancy flux occurs approximately one quarter of the plume thickness below the surface in spreading cases and slightly lower than half the plume thickness in channelized cases. All profiles decrease to zero at the ambient water interface, and are forced to be zero at the water surface. This profile shape is consistent with field observations from the Fraser (MacDonald and Geyer 2004) and Merrimack (MacDonald et al. 2007) river plumes. The buoyancy flux profiles generally have a higher peak in the channelized cases than in the spreading cases, especially for the high flow rate runs. In the channelized cases the turbulent buoyancy flux decreases to zero right at the plume base ($z/H_p = -1$), while in the spreading cases it decreases to zero around $z/H_p = -0.8$.

The depth averaged buoyancy flux over the plume layer is defined as $\bar{B} = \frac{1}{H_p}\int_{-H_p}^{0} B(z)dz$. The average flux is then normalized to form the mixing parameter $\xi = \frac{\bar{B}}{\Delta u g'}$, where Δu is the velocity difference between upper and lower layers. In our case, $\Delta u = U_m$ because there is no velocity in the ambient water. Because the shapes of the profiles are similar, the relationship between B values in different experiments is similar if we use the maximum flux $B_{\max}$ instead of the depth averaged value $\bar{B}$. The value of ξ increases with Fr_i as expected (Figure 11a). Most importantly, however, there is no difference between the values of ξ in spreading and channelized cases (Figure 11a). The average value of ξ is $(1.0 \pm 0.7) \times 10^{-4}$ in the spreading cases and $(1.4 \pm 1.0) \times 10^{-4}$ in the channelized cases. This somewhat surprising result is evidence that local turbulent mixing processes are unaffected by plume spreading.

One significant difference between spreading and channelized cases is that the horizontal surface area of the plume is much higher in spreading cases (Figure 4a). The plume area is two to six times larger in the spreading cases than in the channelized cases (Figure 11b). In order to account for effect of interfacial area on the total mixing, we define the area-integrated turbulent buoyancy flux $\xi_A = \xi\frac{A_S}{A_C}$, where A_S and A_C are the horizontal surface areas in a given spreading run and the corresponding channelized run with similar inflow conditions, respectively. To compare, the area-integrated turbulent buoyancy flux in channelized runs is defined as $\xi_A = \xi \frac{A_C}{A_C}$. In the spreading runs ξ_A is about $2 \sim 6$ times larger than the channelized cases (Figure 11c). The average value of ξ_A is $(4.4 \pm 3.3) \times 10^{-4}$ in the spreading cases and $(1.4 \pm 1.2) \times 10^{-4}$ in the channelized cases. Thus spreading increases the total turbulent mixing, even though it does not appear to change the local mixing processes.

4. Discussion

The results from the present experiments support the conclusion that lateral spreading significantly modifies the plume's vertical structure (Figure 6) and the plume density anomaly (Figure 7). However, these experiments do not support the hypothesis that lateral spreading increases the local mixing, as quantified by the entrainment rate (Figure 9b) or the turbulent buoyancy flux (Figure 11a). We observed increased mixing in the spreading cases compared with the channelized experiments (Figure 11c), but this is shown to be the result of the increased interfacial surface area of the spreading plumes (Figure 11b), rather than any impact of spreading on the local mixing processes.

The results of the present experiments motivate the following question: why doesn't lateral spreading impact turbulent mixing in the plume, even when it significantly modifies the vertical plume structure? We investigate two possible mechanisms that may explain this result in §4.b. Prior to this, we compare the non-dimensional mixing scales observed in the experiments with those of full-scale plume in order to investigate the applicability of the results.

a. Applicability of the laboratory experiments to river plumes

Here we use three non-dimensional parameters for comparing the turbulent mixing in the laboratory simulations, field observations and numerical models:

$$I = \frac{\varepsilon}{\nu N^2}; \qquad \eta = \frac{L_o}{H_p}; \qquad \xi = \frac{\bar{B}}{\Delta u g'}; \tag{12}$$

The first parameter, I, commonly referred to as the buoyancy Reynolds number, can be interpreted as the ratio of the destabilizing effects of turbulent stirring to the stabilizing effects resulting from the combined action of buoyancy and viscosity (Ivey et al. 2008). When I is above a threshold value of $20-30$ the turbulence in the stratified fluid can be maintained (Stillinger et al. 1983). Shih et al. (2005) suggest three discernible regimes of turbulent flow based on their DNS results: a diffusive regime where $I < 7$; an intermediate regime where $7 < I < 100$; and an energetic regime where $I > 100$.

The turbulent kinetic energy dissipation rate ε could not be measured directly in our experiments. In order to estimate an approximate value for ε we assume the turbulent field is homogeneous and isotropic and the flux Richardson number $Ri_f = B/P$ is at its maximum value 0.2. This assumption is valid in stratified shear flow, when the Kelvin-Helmholtz billows are the primary mechanism of turbulence generation (MacDonald and Geyer 2004). With these assumptions we can estimate ε based on the difference between the production and buoyancy flux, ($\varepsilon = \frac{1}{1-Ri_f}\bar{B}$). The values in our experiments range from 10^{-5} to 10^{-4} m^2/s^3, which are typical of observations in stratified coastal environments (Orton and Jay 2005; MacDonald et al. 2007) and one order of magnitude smaller than the lift-off zone in Fraser River plume (MacDonald and Geyer 2004).

The present results for I are plotted in figure 12a, with two thresholds delineating the three regimes indicated by a dashed line ($I = 10$) and dash-dot line ($I = 100$). One of the low Fr_i spreading runs falls in the diffusive regime where the flow is mostly dominated by molecular diffusivity. Most of the data are in the transition or energetic regime in the range of $10 < I < 1000$. They are slightly higher than previous laboratory experiments by Ivey and Imberger (1991) of I between approximately 10 and 100. Field observations have suggested values of I are on the order of 10^4 to 10^5 in the highly stratified Columbia River estuary during ebb tide (Kay and Jay 2003) and in the Fraser River plume (MacDonald and Geyer

2004). In the Connecticut River estuary Geyer et al. (2010) estimated that $I = 100 - 500$. Thus the range of values of I achieved in the laboratory experiments are on the low end of the range observed in natural systems. More importantly, the values that we obtain are in the transitional and energetic regimes where we would expect the processes to be similar to larger-scale systems.

Previous studies have suggested that mixing in gravity driven currents is accomplished through the generation of Kelvin-Helmholtz instabilities as density overturns with scales of similar size to the Ozmidov scale, $Lo = (\varepsilon/N^3)^{1/2}$ (MacDonald and Geyer 2004). These overturns are clearly seen in the mixing layer of the plume in both cases (Figure 2 and 3). An important question for the current experiments is whether the thinness of the plume layer limits the scales of turbulent mixing and, in particular, if this effect could differentially influence the mixing in the thinner spreading plume runs. Figure 12b shows estimates of L_o normalized by the plume thickness H_p. The Ozmidov scale L_o is roughly the same size as the plume thickness H_p, i.e., L_o/H_p is on the order of 1. We observe that L_o/H_p increases with Fr_i and that L_o exceeds H_p in a few high Fr_i experiments. This indicates that the plume thickness has the potential to inhibit the turbulence. However, there is no indication that the influence of the plume thickness is greater in the spreading or channelized experiments. Thus we conclude that depth limitation cannot explain the result that the local mixing processes are unaffected by spreading.

Finally, the mixing parameter ξ represents the efficiency with which energy is extracted from the mean flow and converted into turbulent energy (MacDonald and Geyer 2004; MacDonald and Chen 2012). The values of ξ observed in the present experiments are in the range from 10^{-5} to 10^{-3} (Figure 11a). This broad range agrees with results from the Fraser River, where ξ was estimated to be approximately 2.6×10^{-4} (MacDonald and Geyer 2004). The channelized cases can be compared with the non-spreading limit $\xi_0 = 5 \times 10^{-5}$ described in MacDonald and Chen (2012).

Although the Reynolds numbers of the laboratory-generated plumes (Table 1) are significantly lower than most plumes observed in the field, the buoyancy Reynolds number I and the mixing parameter ξ are both in the same approximate range, suggesting that the turbulence is sufficiently active to represent the processes observed in the field. So we conclude that Reynolds number limitation does not appear to influence our findings from the laboratory experiments.

b. Two possible mechanisms

The results presented in §3.c describe important differences in the structure of channelized and spreading currents. The buoyant current in the channelized case has step-wise density and velocity structures, as is commonly observed in the two-layer exchange flow in estuary channels (Figure 13a line in the dark gray area). It has a minimum density (maximum velocity) in the near-surface uniform density layer, a maximum density (zero velocity) in the bottom layer and a mixing layer in between in which the density increases and velocity decreases continuously. In the spreading case, however, the near-surface uniform density layer disappears and the vertical plume structure consists of a $1-1/2$ layer system with a mixing layer that extends approximately linearly to the water surface (Figure 13a line in the light gray area). This structure is consistent with field observations in near-field river plumes (e.g. MacDonald and Geyer (2004); MacDonald et al. (2007); Kilcher et al. (2012)). Despite the difference in the structure of the spreading and channelized currents, the properties of the mixing layer such as the mixing layer thickness, the density structure and the velocity structure are almost identical in both cases for similar inflow conditions. In addition, mixing properties such as the entrainment velocity and turbulent buoyancy flux are similar in the spreading and channelized cases.

We consider two mechanisms that may explain the unexpected result that local mixing processes are not affected by plume spreading. Both invoke the idea that there is vertical structure to the spreading and mixing processes and that the influence of spreading on mixing will be minimized if the two processes are misaligned spatially. The proposed mechanisms leading to this misalignment are different in the region very near the river mouth and in the rest of the near-field plume. They are described below and summarized schematically in Figure 13. First, in the jet-to-plume transition region immediately offshore of the river mouth where the current transforms from a buoyant jet into a river plume, the spreading occurs primarily in the near-surface uniform density region while most mixing occurs at the plume base. Second, although the spreading and mixing occur within the same layer in the near field region, their structures are offset such that spreading does not significantly impact the region of maximum mixing.

1) Jet-to-Plume region

The region near the river mouth is one of the most energetic regions in the river plume. Total mixing in this region is of the same order of magnitude as it is in the mid-field and far-field plumes, even though the near-field is orders of magnitude smaller in area (Hetland and MacDonald 2008). In the spreading case, the flow evolves in this region from a channelized current in the estuary into a buoyant river plume. As the current moves offshore, the density and velocity profiles change dramatically from two-layer step-wise profiles to mixing layer profiles (Figure 13a).

Lateral spreading is due to the horizontal pressure gradient, which is highest at the water surface and decreases to zero at the plume base. Our hypothesis is that in this transition region the spreading occurs preferentially in the near-surface uniform density layer (Figure 13c dark gray area) while the most energetic mixing occurs at the lower layer of the plume (Figure 13c light gray area). Thus, the mixing layer does not experience significant lateral spreading. Instead, the main result of lateral spreading is that the near-surface uniform density layer disappears, as shown in the cartoon of this jet-plume region (Figure 13c).

Jirka et al. (1981) describe the jet-plume region as the region where momentum dominates over buoyancy and the impact of the initial channel geometry disappears. They define a jet-plume length scale as $L_M = (Q_0U_0)^{3/4}/(Q_0g'_0)^{1/2}$. The jet-plume length scale is relatively small compared to the whole plume and is even smaller than the near-field plume scale. In this region the plume behaves much like a buoyant jet, driven by the enhanced velocities of the discharge as it initially enters the coastal region.

In our experiments, the jet-to-plume length scale is 8.8 cm for $g' = 2$ cm/s^2 (3.5 cm for $g' = 5$ cm/s^2). Thus, the location of our PIV-PLIF measurements, which is ≈ 30 cm from the river mouth, is well beyond the jet-to-plume region and we would expect to observe only the fully developed mixing layer profiles. This is consistent with the observed profiles shown in Figure 6. We suggest that spreading within the jet-to-plume region is due primarily to lateral slumping of the initially uniform density surface layer and that mixing, which is primarily at the base of this layer is unaffected.

2) Near-field region

Seaward of the jet-to-plume region, the spreading plumes are characterized by linear density and velocity profiles (Figure 6a). Profiles of vertical buoyancy flux in the spreading cases have maxima at $z \approx -H_p/4$ (Figure 10) and decrease to zero both at the surface and at the plume base.

As discussed in the §4.b.1, lateral spreading is due to a horizontal pressure gradient normal to the plume axis. The pressure gradient (dP/dy) is expected to be a linear function of depth within the plume; highest at the water surface and decreasing to zero at the plume base. Although we cannot directly calculate the spreading rate based on the horizontal pressure gradient, it is reasonable to assume the spreading rate should have the same shape as the pressure gradient.

In addition, we can calculate the local lateral spreading rate (dv/dy) along the plume axis directly from the measured velocity field based on the continuity equation:

$$\frac{dv}{dy} = -(\frac{du}{dx} + \frac{dw}{dz}). \tag{13}$$

The local lateral spreading profile is calculated by averaging the dv/dy field horizontally over 12 cm and then normalizing it by its maximum value. In Figure 14 the normalized spreading rate is plotted against the normalized vertical axis and fitted by an exponential curve to compare with the normalized buoyancy flux profiles. The lateral spreading rate has its maximum value at the water surface and is highest within the top half of the layer. It decreases dramatically in the lower half of plume layer. Meanwhile, the mixing profile has its maximum at $z \approx -H_p/4$ and decreases both upward and downward. The spreading rate at the location of the maximum buoyancy flux is between 20% to 50% of the maximum spreading rate at the surface. Throughout the lower three-quarters of plume layer lateral spreading is significantly reduced and is not expected to influence mixing. This lower three-quarters of the layer is where the entrainment generates the greatest turbulent buoyancy flux because the density gradient is high, i.e., entraining dense fluid from the ambient water ($w_e > 0$) in Figure 8.

This mechanism is similar to the mechanism described for the jet-to-plume region; the maxima in the spreading and mixing profiles are not coincident. The spreading at the top unmixed layer and mixing (entrainment) at the plume base with no overlap in the jet-to-plume region is the extreme case of the offset mixing and spreading profiles discussed here (Figure 13b).

The lateral spreading rate is commonly known to be related to the local internal gravity wave speed, i.e., $\sqrt{g'h}$ (Wright and Coleman 1971; Hetland and MacDonald 2008). In our experiments and in previous studies that use the control volume method, the lateral spreading rate is assumed to be independent of depth (MacDonald and Geyer 2004; Kilcher et al. 2012). This assumption agrees reasonably well with field data, although authors have hypothesized that observed discrepancies may be attributed to the depth dependence in the spreading. Our analysis supports this hypothesis; suggesting that the vertical structure of lateral spreading rate actually may play an important role in determining the relationship between lateral spreading and its effect on mixing.

5. Conclusion

This paper presents a direct comparison between channelized and freely spreading buoyant gravity currents with a continuous freshwater source. The configuration of the laboratory experiments simulates a coastal river inflow with a simplified geometry in order to better understand the role of lateral spreading on the mixing and dilution of river water as it enters the coastal ocean.

Consistent with predictions from previous work (Wright and Coleman 1971; Hetland and MacDonald 2008), we observe that the lateral spreading rate is highly dependent on the inflow condition as characterized by Fr_i: the plume is convergent when $Fr_i < 1$ and divergent when $Fr_i > 1$ (Figure 5). As a consequence of these changes to the spreading rate, the increase in plume area due to spreading within a given distance from the river mouth is significantly greater for low Fr_i than high Fr_i plumes (Figure 11b).

Lateral spreading dramatically modifies the plume's vertical structure; the spreading plumes consist of approximately linear density and velocity profiles that extend to the surface, whereas the channelized plumes have regions of uniform density and velocity near the surface (Figure 6). In addition, the average density of the plume layer at a fixed distance from the river mouth is higher in the spreading experiments than in the channelized experiments (Figure 7).

We estimate the entrainment rate E and the turbulent buoyancy flux B using the control volume method described by MacDonald and Geyer (2004). The entrainment rate is at the same order of magnitude as the previous laboratory studies. It fits the $Ri_b^{-1/2}$ law (Ellison and Turner 1959; Christodoulou 1986) in the low Ri_b region. A key outcome of this work is the observation that there is no difference in the entrainment rate or buoyancy flux between the channelized and spreading cases. This indicates that lateral spreading does not modify the local mixing efficiency, counter to the expectations outlined in MacDonald and Chen (2012). We hypothesize that this is because the spreading occurs preferentially near the surface, whereas buoyancy flux is greatest in the core of the current.

We conclude that spreading significantly increases the total mixing in the plume (Figure 11c). However, the increase in mixing is due to the increase in the area of the plume (Figure 11b) as opposed to changes in the local mixing processes associated with spreading (Figure 11a). As estuary water enters the coastal ocean, lateral expansion occurs preferentially near the surface, eliminating the uniform density layer observed at the surface in the estuary and shifting the mixing layer upwards to the water surface. Near-surface water is thus redistributed across a much wider area, where it then forms the plume base and is susceptible to mixing. The result of the lateral advection of fresh near-surface water is that the plume layer is more diluted on average in the presence of spreading than an equivalent channelized flow.

Acknowledgments.

The authors would like to thank three undergraduate students, Anthony Poggioli, Amanda Gehman and Stephanie Wei, who helped with the experiments. We would also like to thank D. MacDonald, R. Hetland and the other members of the MeRMADE project team whose discussions of the work and earlier reviews of this manuscript are very helpful. Finally, the authors are grateful to NSF for support of the project through grant OCE-0850847. The authors gratefully acknowledges suggestions from the anonymous reviewers that greatly improved the manuscript.

REFERENCES

Benjamin, T. B., 1968: Gravity currents and related phenomena. *J. Fluid. Mech.*, **31**, 209–248.

Britter, R. E. and J. E. Simpson, 1978: Experiments on the dynamics of a gravity current head. *J. Fluid Mech.*, **88**, 223–240.

Buch, E., 1980: On entrainment and vertical mixing in stably stratified fjords. *2nd Intern. Symposium on Stratified flows*, Throndheim, Norway, 461–469.

Cantero, M. I., S. Balachandar, and M. H. Gacia, 2007: High-resolution simulations of cylindrical density currents. *J. Fluid Mech.*, **590**, 437–469.

Cantero, M. I., S. Balachandar, M. H. Gacia, and J. Ferry, 2006: Direct numerical simulations of planar and cylindrical density currents. *J. Appl. Mech.*, **73**, 923–930.

Cenedese, C. and S. Dalziel, 1998: Concentration and depth field determined by the light transimitted through a dyed solution. *8th International symposium on flow visualization*, 61.1 – 61.5.

Chen, F., D. G. MacDonald, and R. D. Hetland, 2009: Lateral spreading of a near-field river plume: Observations and numerical simulations. *J. Geophys. Res.*, **114**, C07 013, doi:10.1029/2008JC004893.

Chen, J. C., 1980: Studies on gravitational spreading currents. Ph.D. thesis, California Institute of Technology, 436 pp.

Christodoulou, G. C., 1986: Interfacial mixing in stratified flows. *J. Hydraul. Res.*, **24 (2)**, 77–92.

Chu, V. H. and M. R. Vanvari, 1976: Experimental study of turbulent stratified shearing flow. *J. Hydraulics Div., ASCE*, **102 (HY6)**, 691–706.

Cowen, E., K. A. Chang, and Q. Liao, 2001: A single camera coupled PTV-LIF technique. *Exp. Fluids*, **31 (1)**, 63–73.

Crimaldi, J. P., 2008: Planar laser induced fluorescence in aqueous flows. *Exp. Fluids*, **44 (6)**, 851–863.

Didden, N. and T. Maxworthy, 1982: The viscous spreading of plane and axisymmetric gravity currents. *J. Fluid Mech.*, **121**, 27–42.

Ellison, T. H. and J. S. Turner, 1959: Turbulent entrainment in stratified flows. *J. Fluid Mechanics*, **6**, 423–448.

Garvine, R. W. and J. D. Monk, 1974: Frontal structure of a river plume. *J. Geophys. Res.*, **79 (15)**, 2251–2259.

Geyer, W. R., A. C. Lavery, M. E. Scully, and J. H. Trowbridge, 2010: Mixing by shear instability at high Reynolds number. *Geophys. Res. Lett.*, **37**, L22 607.

Hallworth, M. A., H. E. Huppert, J. C. Phillips, and R. S. J. Sparks, 1996: Entrainment into two-dimensional and axisymmetric turbulent gravity currents. *J. Fluid Mech.*, **308**, 289–311.

Hartel, C., E. Meiburg, and F. Necker, 2000: Analysis and direct numerical simulation of the flow at a gravity-current head. Part 1. Flow topology and front speed for slip and non-slip boundaries. *J. Fluid Mech.*, **418**, 189–212.

Hetland, R. D., 2010: The effects of mixing and spreading on density in near-field river plumes. *Dyn. Atmos. Oceans*, **49**, 37–53.

Hetland, R. D. and D. G. MacDonald, 2008: Spreading in the near-field merrimack river plume. *Ocean Modell.*, **21**, 12–21, doi:10.1016/j.ocemod.2007.11.001.

Horner-Devine, A. R., 2006: Velocity, density and transport measurements in rotating, stratified flows. *Exp. Fluids*, **41 (4)**, 559–571.

Huppert, H. E. and J. E. Simpson, 1980: The slumping of gravity currents. *J. Fluid Mech.*, **99**, 785–799.

Ivey, G. N. and J. Imberger, 1991: On the nature of turbulence in a stratified fluid: 1. The energetics of mixing. *J. Phys. Oceanogr.*, **21**, 650–658.

Ivey, G. N., K. B. Winters, and J. R. Koseff, 2008: Density stratification, turbulence, but how much mixing? *Annu. Rev. Fluid Mech.*, **40**, 169–84.

Jirka, G. H., E. E. Adams, and K. D. Stolzenbach, 1981: Buoyant surface jets. *J. Hydr. Div*, **107 (11)**, 1467–1487.

Kay, D. J. and D. A. Jay, 2003: Interfacial mixing in a highly stratified estuary 1. Characteristics of mixing. *J. Geophys. Res.*, **108 (C3)**, 3072.

Kilcher, L. F. and J. D. Nash, 2010: Structure and dynamics of the Columbia River tidal plume front. *J. Geophys. Res.*, **115**, C05S90.

Kilcher, L. F., J. D. Nash, and J. N. Moum, 2012: The role of turbulence stress divergence in decelerating a river plume. *J. Geophys. Res.*, **117**, C05 032.

Lawrence, G. A., F. K. Browand, and L. G. Redekopp, 1991: The stability of a sheared density interface. *Phys. Fluids*, **3 (10)**, 2360–2370.

Luketina, D. A. and J. Imberger, 1987: Characteristics of a surface buoyant jet. *J. Geophys. Res.*, **94 (C5)**, 5435–5447.

MacDonald, D. G. and F. Chen, 2012: Enhancement of turbulence through lateral spreading in a stratified-shear flow: Development and assessment of a conceptual model. *J. Geophys. Res.*, inpress, doi:10.1029/2011JC007484.

MacDonald, D. G. and W. R. Geyer, 2004: Turbulent energy production and entrainment at a highly stratified estuarine front. *J. Geophys. Res.*, **109**, C05 004, doi:10.1029/2003JC002094.

MacDonald, D. G. and A. R. Horner-Devine, 2008: Temporal and spatial variability of vertical salt flux in a highly stratified estuary. *J. Geophys. Res.*, **113**, C09 022, doi:10.1029/2007JC004620.

MacDonald, M. D., L. Goodman, and R. D. Hetland, 2007: Turbulent dissipation in a near-field river plume: A comparison of control volume and microstructure observations with a numerical model. *J. Geophys. Res.*, **112**, C07 026, doi:10.1029/2006JC004075.

Morton, B. R., G. Taylor, and J. S. Turner, 1956: Turbulent gravitational convection from maintained and instantaneous sources. *Proc. R. Soc. London, Ser. A*, **234**, 1–23.

Nowacki, D. J., A. R. Horner-Devine, J. D. Nash, and D. A. Jay, 2012: Rapid sediment removal from the columbia river plume near field. *Continental Shelf Research*, **35**, 16–28.

Orton, P. M. and D. A. Jay, 2005: Observations at the tidal plume front of a high-volume river outflow. *Geophys. Res. Lett.*, **32**, L11 605.

Patterson, M. D., J. E. Simpson, S. B. Dalziel, and G. J. F. van Heijst, 2006: Vortical motion in the head of an axisymmetric gravity current. *Phys. Fluids*, **18**, 046 601.

Pedersen, F. B., 1980: *A Monograph on turbulent entrainment and friction in two-layer stratified flow.* Inst. of Hydrodynamics and Hydraulic Engin., Techn. University of Denmark, Series Paper No. 25.

Rocca, M. L., C. Adduce, G. Sciortino, and A. B. Pinzon, 2008: Experimental and numerical simulation of three-dimensional gravity currents on smooth and rough bottom. *Phys. Fluids*, **20**, 106 603.

Shih, L. H., J. R. Koseff, G. N. Ivey, and J. H. Ferziger, 2005: Parameterization of turbulent fluxes and scales using homogenous sheared stably stratified turbulence simulations. *J. Fluid Mech.*, **525**, 193–214.

Shin, J. O., S. B. Dalziel, and P. F. Linden, 2004: Gravity currents produced by lock exchange. *J. Fluid Mech.*, **521**, 1–34.

Simpson, J. E., 1997: *Gravity Current: in the Environment and the Laboratory*. 2d ed., Cambridge University Press, 244 pp.

Stillinger, D. C., K. N. Helland, and C. W. V. Atta, 1983: Experiments on the transition of homogeneous turbulence to internal waves in a stratified fluid. *J. Fluid Mech.*, **131**, 91–122.

Sveen, J. K., 2004: An introduction to matpiv v.1.6.1. Eprint no. 2, **ISSN** 0809-4403, Dept. of Mathematics, University of Oslo, 27 pp.

Tedford, E. W., J. R. Carpenter, R. Pawlowicz, R. Pieters, and G. A. Lawrence, 2009a: Observation and analysis of shear instability in the fraser river estuary. *J. Geophys. Res.*, **114**, C11 006.

Tedford, E. W., R. Pieters, and G. A. Lawrence, 2009b: Symmetric holmboe instabilities in a laboratory exchange flow. *J. Fluid Mech.*, **636**, 137–153.

Thomas, L. P., S. B. Dalziel, and B. M. Marino, 2003: The structure of the head of an inertial gravity current determined by particle-tracking velocimetry. *Exp. Fluids*, **34**, 708.

Thorpe, S. A., 1971: Experiments on instability of stratified shear flow: miscible fluids. *J. Fluid Mech.*, **46**, 299–319.

Thorpe, S. A., 1973: Experiments on instability and turbulence in a stratified shear flow. *J. Fluid Mech.*, **61**, 731–751.

Ungarish, M. and T. Zemach, 2005: On the slumping of high reynolds number gravity currents in two-dimensional and axisymmetric configurations. *Eur. J. Mech. B/Fluids*, **24**, 71–90.

von Karman, T., 1940: The engineer grapples with nonlinear problems. *Bull. Amer. Math. Soc.*, **46**, 615–683.

Wright, L. D. and J. M. Coleman, 1971: Effluent expansion and interfacial mixing in the presence of a salt wedge, Mississippi River Delta. *J. Geophys. Res.*, **76 (36)**, 8649–8661.

Yuan, Y., M. E. Averner, and A. R. Horner-Devine, 2011: A two-color optical method for determining layer thickness in two interacting buoyant plumes. *Exp. Fluids*, **50 (5)**, 1235–1245.

List of Tables

Table 1. The parameters of the experiments.

	g'_0(cm^2/s)	Q_0(gpm)	U_0(cm/s)	Fr_i	Re
SP1	2.11	6	2.52	0.78	7568
SP2	2.01	9	3.78	1.19	11352
SP3	1.80	12	5.05	1.68	15136
SP4	1.74	15	6.31	2.14	18920
SP5	5.05	6	2.52	0.50	7568
SP6	5.28	9	3.88	0.74	11352
SP7	5.40	12	5.05	0.97	15136
SP8	5.64	15	6.31	1.19	18920
CH1	2.13	6	2.52	0.73	7277
CH2	2.35	9	3.78	1.29	12613
CH3	2.22	12	5.05	1.43	14554
CH4	2.34	15	6.31	1.84	18920
CH5	5.38	6	2.52	0.49	7568
CH6	5.20	9	3.78	0.79	11825
CH7	4.97	12	5.05	1.01	15136
CH8	5.02	15	6.31	1.26	18920
PL1	2.40	5	2.15	0.62	6459
PL2	2.01	9	3.88	1.19	11352
PL3	2.64	12	5.05	1.39	15080
PL4	1.80	12	5.05	1.68	15136
PL5	9.13	4	1.68	0.25	5045
PL6	5.05	6	2.52	0.5	7568
PL7	4.05	6	2.52	0.56	7532
PL8	5.27	8	3.44	0.67	10334
PL9	5.28	9	3.88	0.74	11352
PL10	5.64	15	6.31	1.19	18920

List of Figures

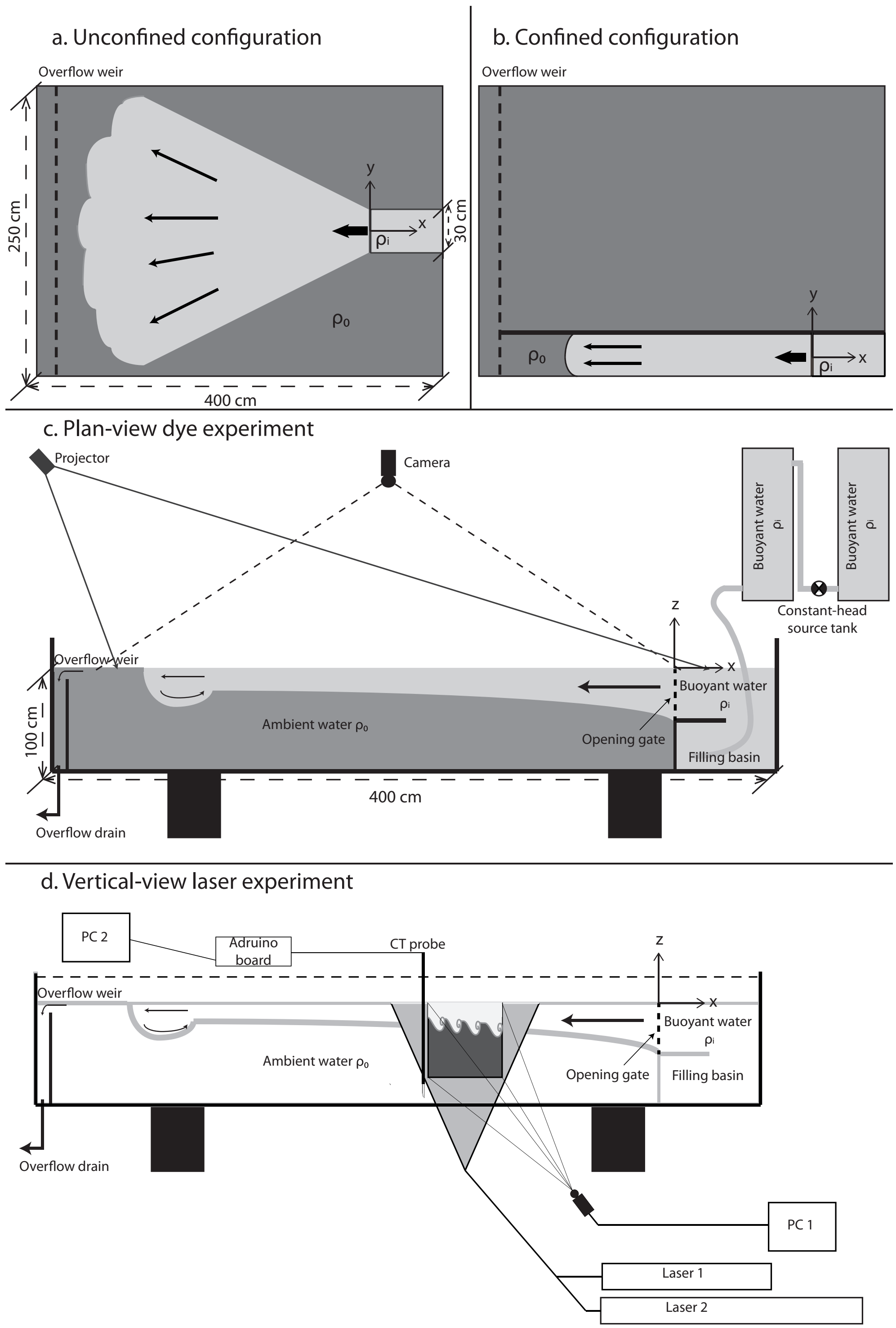

FIG. 1. Schematic of laterally a) unconfined (spreading) and b) confined (channelized) gravity currents and schematics of experimental facility and instrumentation for c) the plan-view dye experiments and d) vertical-view laser experiments. The Cartesian coordinate is defined in the schematic: origin is at the center of the river mouth water surface, x is the onshore coordinate, y is the alongshore coordinate, z is the vertical coordinate with positive upward.

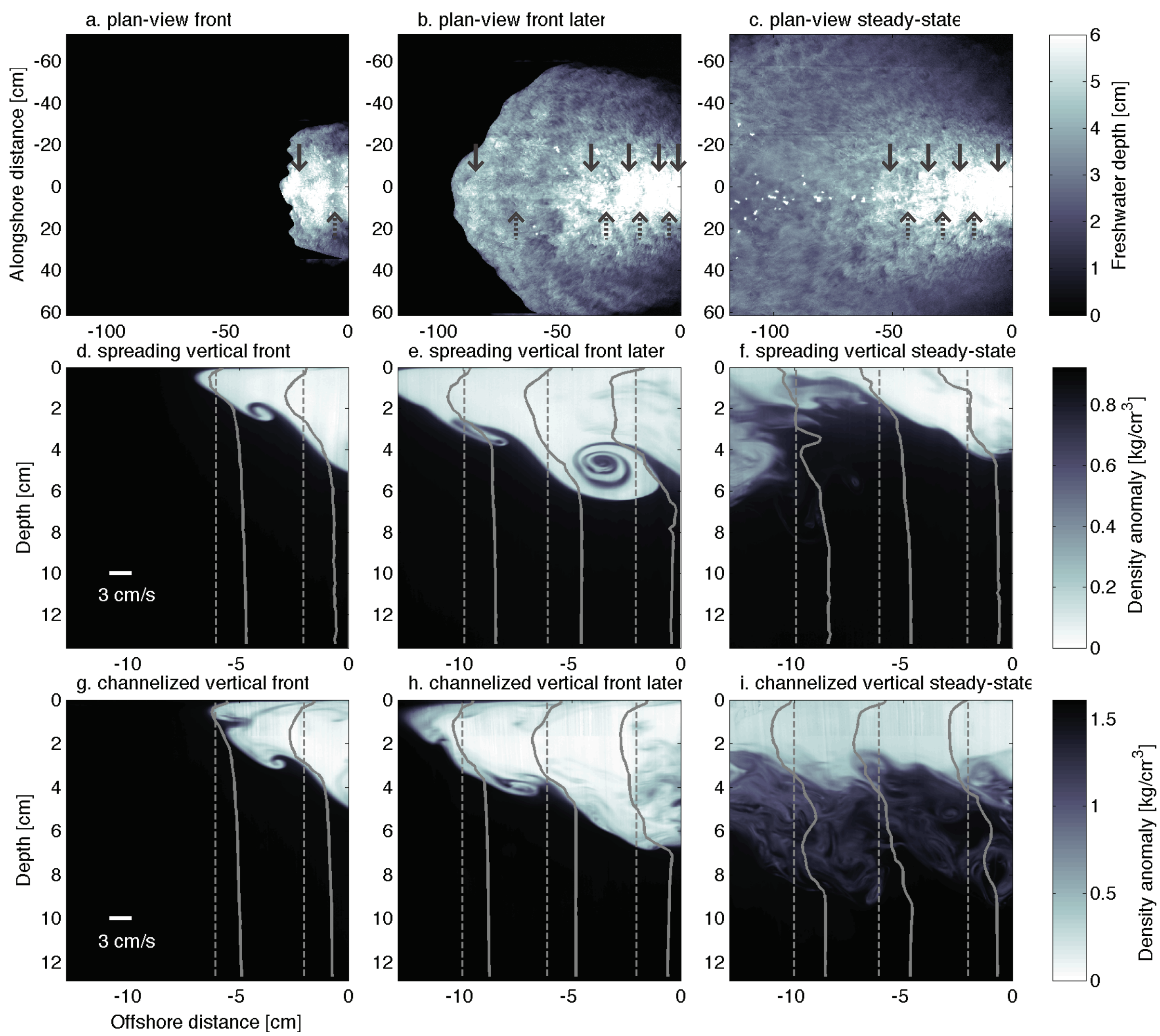

FIG. 2. High Fr_i spreading ($Fr_i = 1.68$) and channelized ($Fr_i = 1.43$) runs. Plan-view freshwater thickness fields from the spreading run PL4 (a-c), density field with superimposed front-relative velocity profiles from the spreading run SP3 (d-f), and density field with superimposed front-relative velocity profiles from the corresponding channelized run CH3 (g-i). Solid arrows in subplots a-c point the frontal bore and brighter bands, while dash arrows point darker bands. Dash lines in d-i are zero velocity lines and velocity scale bars are in subplots d and g.

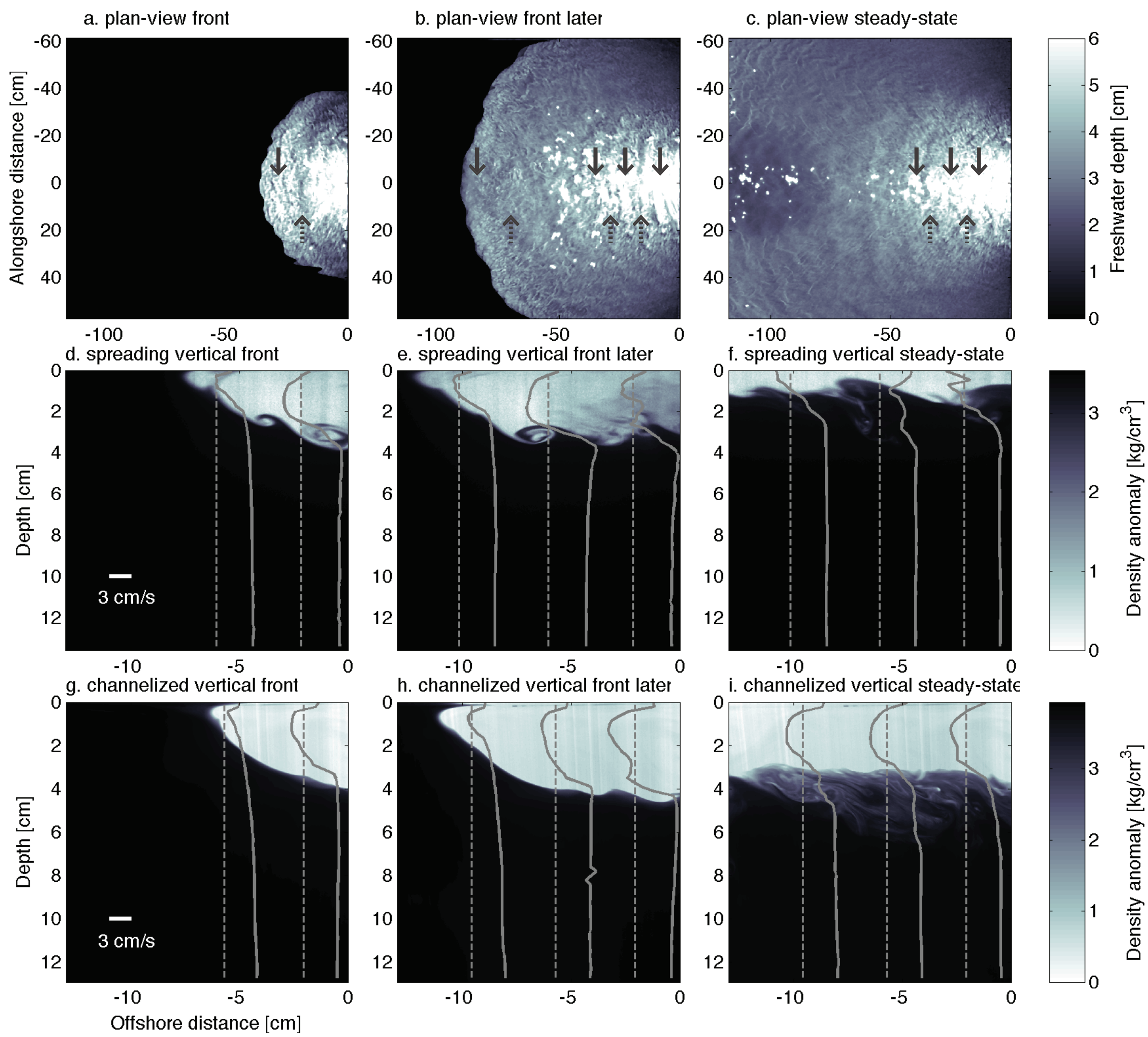

FIG. 3. Same as Figure 2 but for low Fr_i runs (SP5/PL6: $Fr_i = 0.50$ and CH5: $Fr_i = 0.49$).

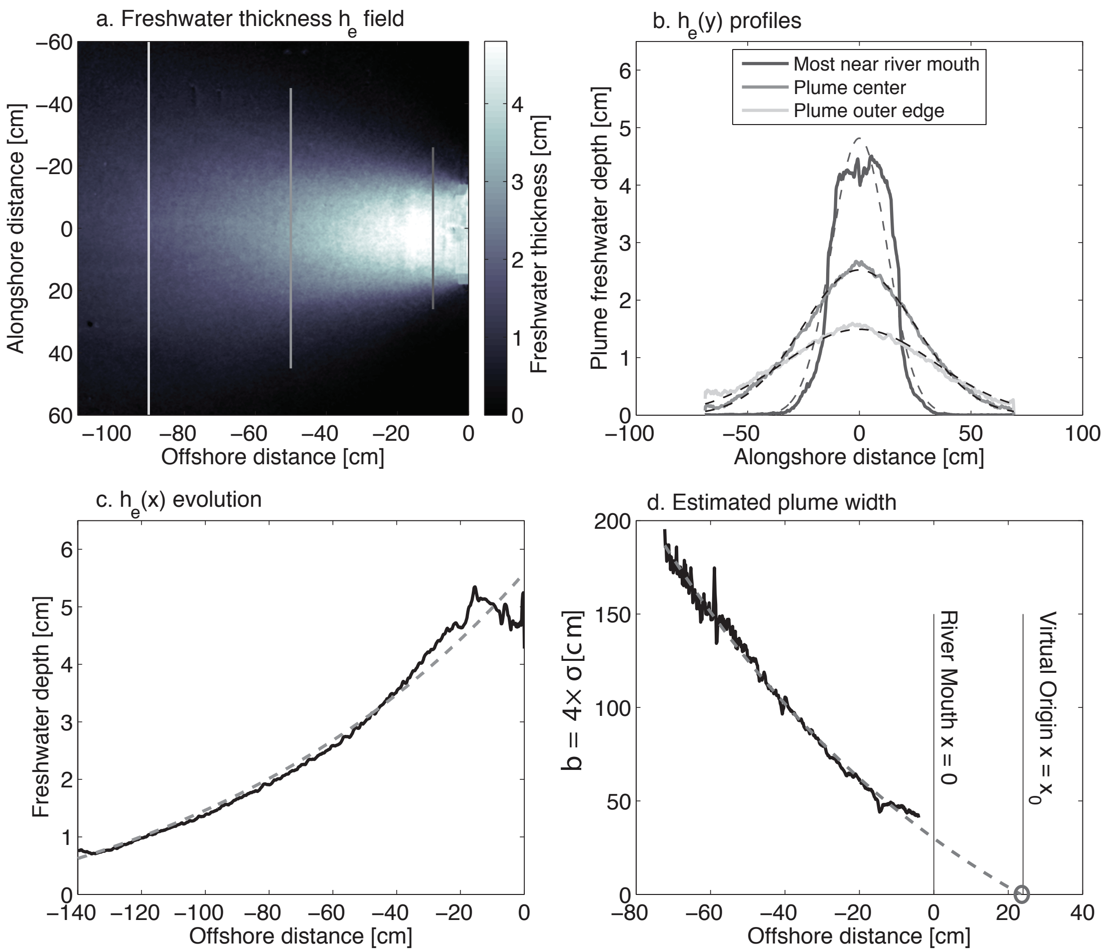

FIG. 4. a) Time averaged plan-view freshwater thickness h_e field, b) $h_e(y)$ profiles at the three cross-sections shown in panel a) (dashed lines are the Gaussian fit to each profiles), c) $h_e(x)$ evolution along the plume center line ($y = 0$) (dash line is the exponential fit), and d) estimated plume width defined as $b = 4 \times \sigma$ based on Gaussian fit of $h_e(y)$ (dash line is the exponential fit) for a high Fr_i spreading run (PL4: $Fr_i = 1.68$; Figure 2a-c). The two black lines in panel d) indicate the river mouth $x = 0$ and the virtual origin $x = x_0$.

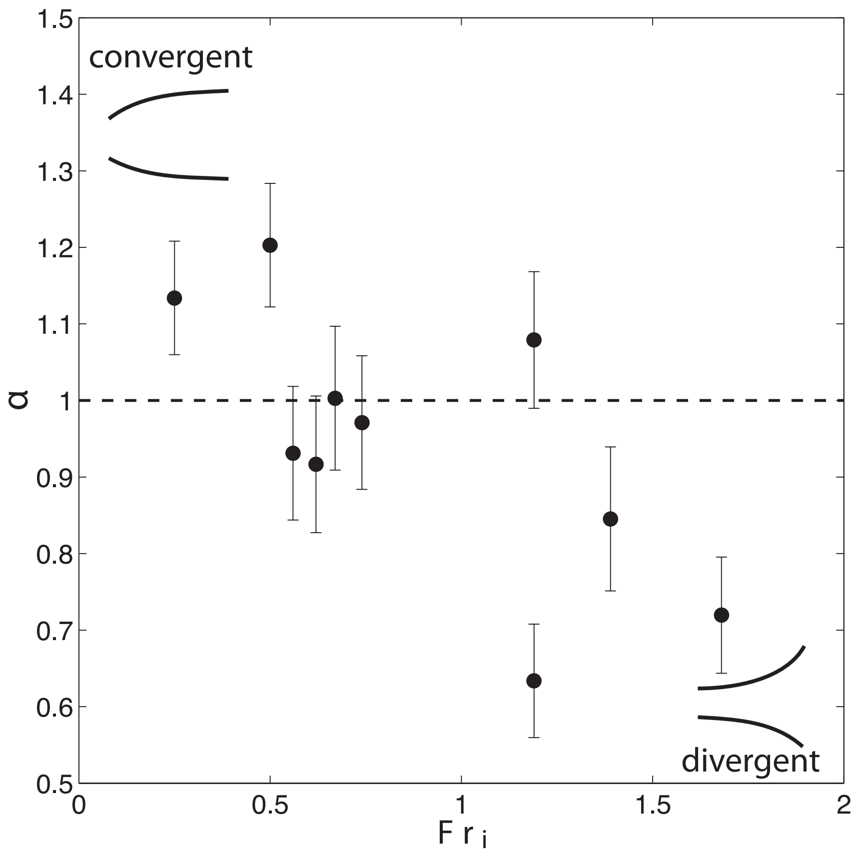

FIG. 5. Plot of spreading rate α vs. Fr_i. The dash line is $\alpha = 1$, indicating the pure radial spreading $u/\delta = x$. Schematic representations of convergent and divergent plumes, adopted from Hetland and MacDonald (2008), are shown above and below the $\alpha = 1$ line. Error bars are estimated based on the exponential fit to the width data.

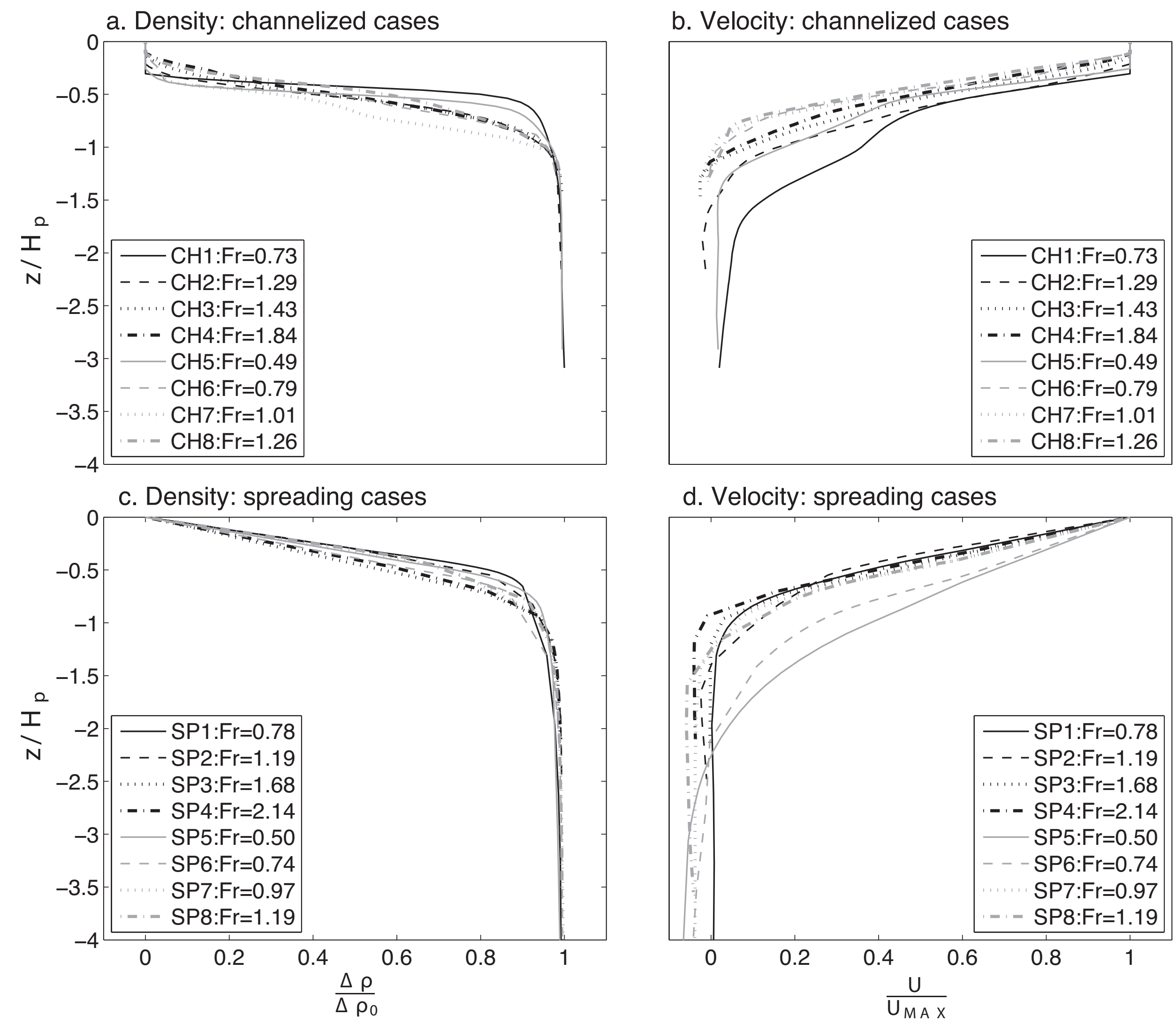

Fig. 6. Normalized density (a and c) and horizontal velocity (b and d) profiles for channelized (upper) and spreading (lower) runs. Detailed parameters of each runs shown in the legend are in Table 1. Vertical axis is normalized by the plume thickness (H_p), which is defined as the depth of the 95% freshwater flux contour.

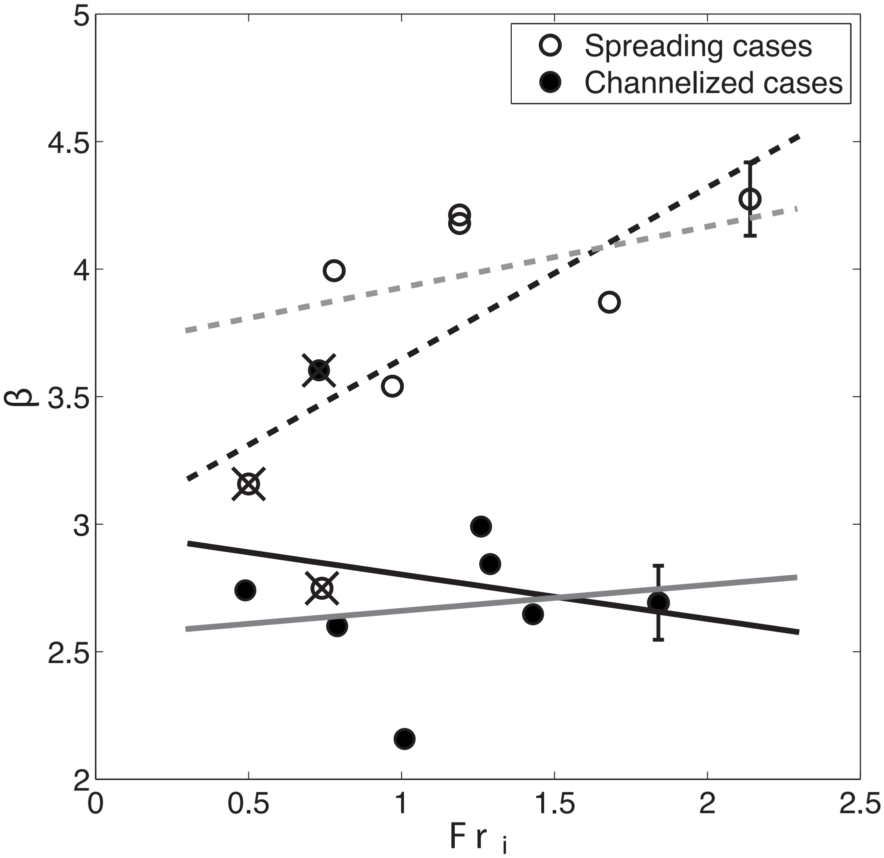

FIG. 7. Buoyancy anomaly (β) vs. Fr_i for spreading (open circles) and channelized (filled circles) runs. The averaged error bars for each configuration are plotted at the highest Fr_i points. Black dash line and black solid line are the linear fits to the spreading and channelized runs, respectively. Cross symbols highlight three points (SP5, SP6, and CH1) with opposite result comparing to other runs. Shaded dash line and shaded solid line are the linear fits without three anomalous points to the spreading and channelized runs, respectively. Two low Fr_i spreading runs (SP5 and SP6) have mis-matched density and velocity profiles (Figure 6). They are not within the same range as the other points in their group, and may reflect a different mixing regime. The reason for anomalous result of the low Fr_i channelized run (CH1) is unclear.

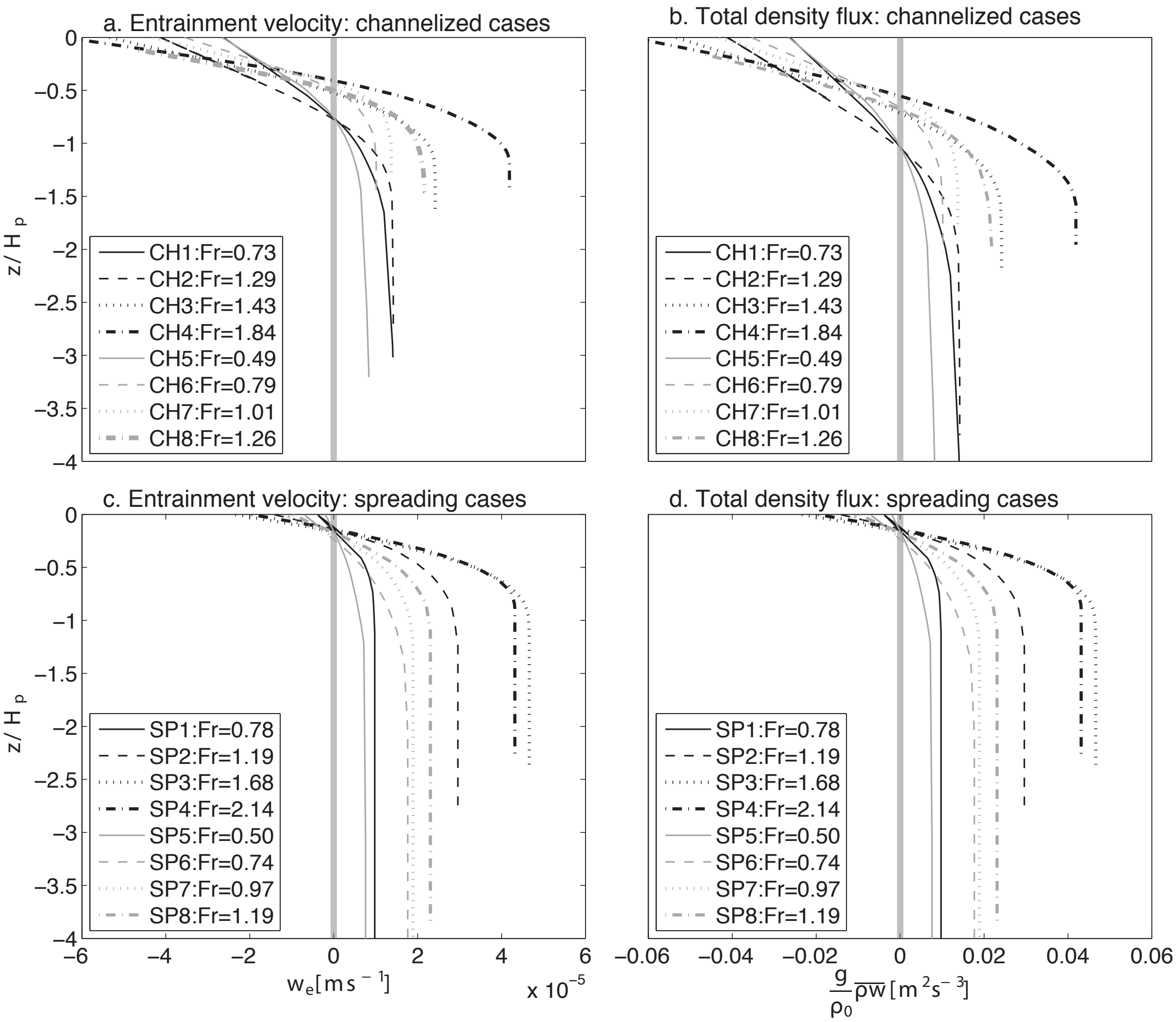

FIG. 8. Plume entrainment velocity w_e (a and c) and total vertical density flux $\frac{g}{\rho_0}\overline{\rho w}$ (b and d) for channelized (upper) and spreading (lower) experiments. The vertical thick shaded lines indicate the zero value of entrainment velocity or total vertical density flux in each panel.

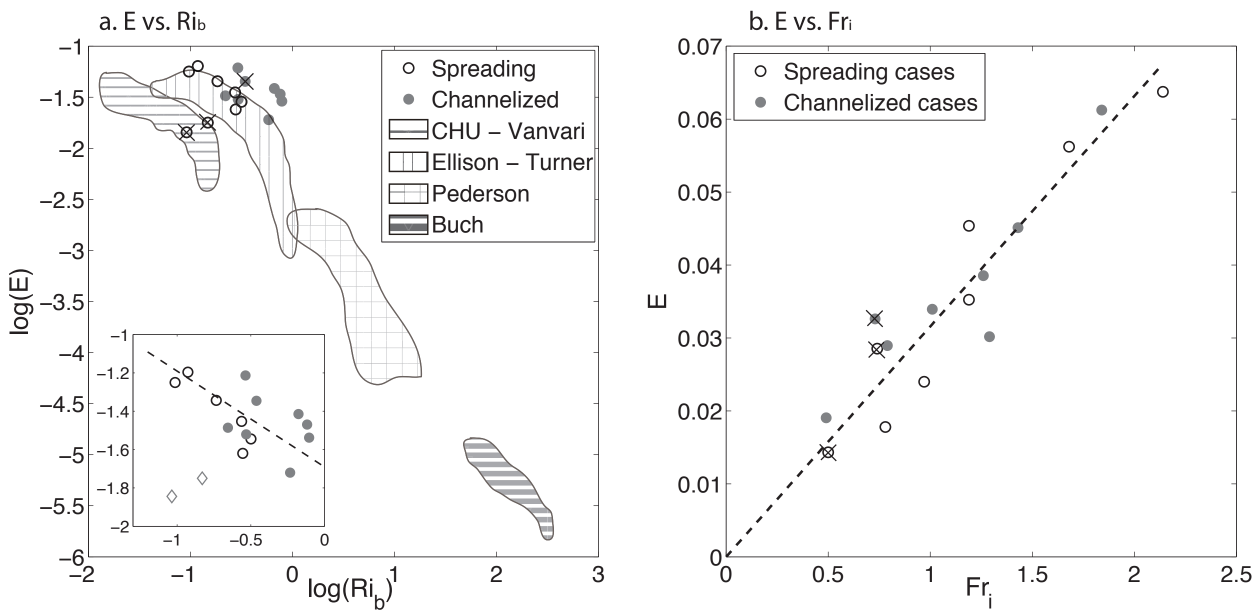

FIG. 9. a) Entrainment rate (E) vs. bulk Richardson number (Ri_b). Data represented by the shaded regions are drawn from Christodoulou (1986) with the data from laboratory experiments by Chu and Vanvari (1976); Ellison and Turner (1959); Pedersen (1980) and field observation by Buch (1980). The insert of (a) is the zoom-in of data from present experiments. The dash line is the fit to $E = 0.02Ri_b^{-1/2}$ law to all data as suggested by Christodoulou (1986) (excluding the two low Fr_i runs indicated with diamonds). b) Entrainment rate (E) vs. inflow Froude number (Fr_i) for spreading and channelized cases. The dashed line corresponds to $E = 0.03Ri_{bi}^{-1/2}$. Cross symbols highlight three points (SP5, SP6, and CH1) discussed in Figure 7.

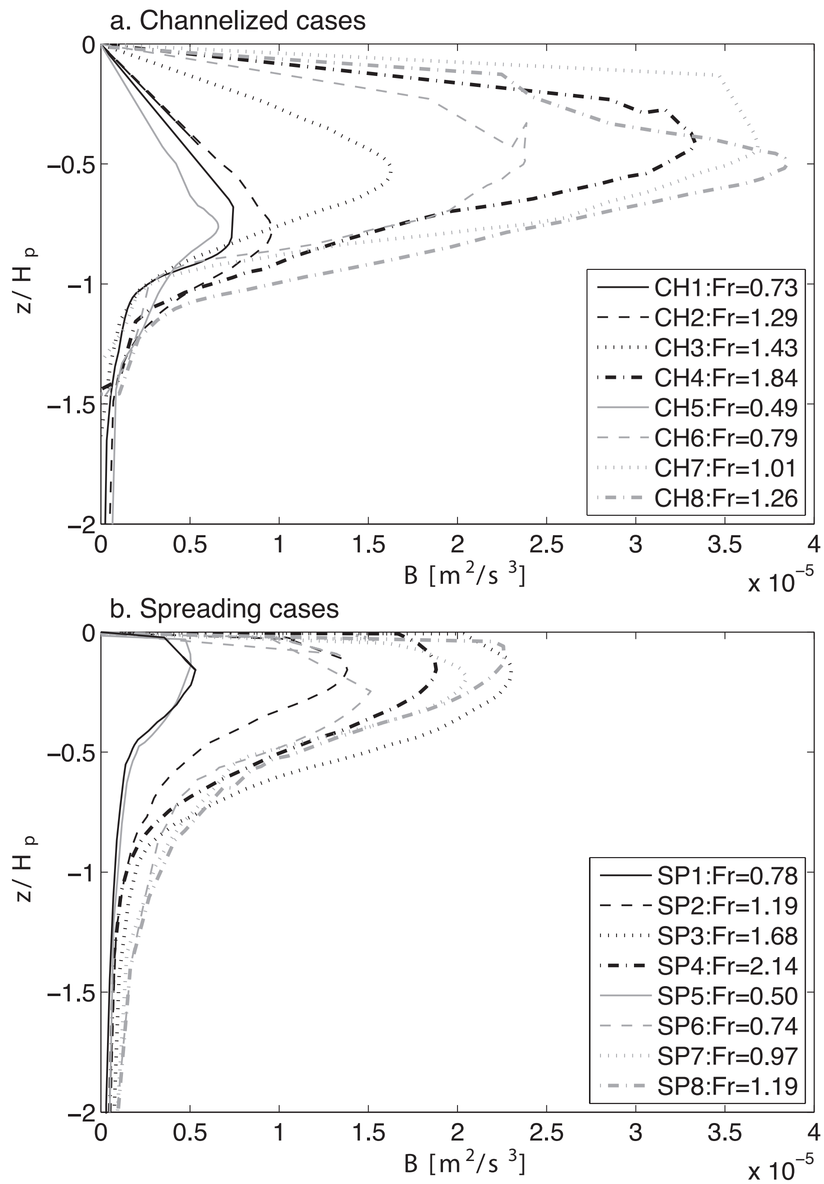

Fig. 10. Turbulent buoyancy flux profile estimated using the control volume method for a) channelized and b) spreading runs.

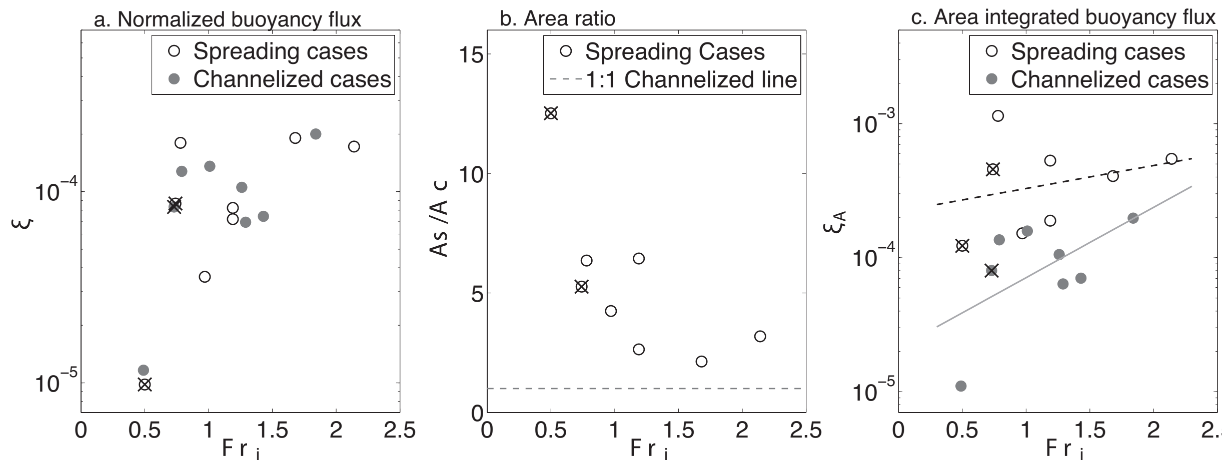

FIG. 11. a) Normalized buoyancy flux $\xi = \frac{\bar{B}}{\Delta u g'}$, b) ratio of plume area in spreading cases (A_S) to channelized cases (A_C), and c) area-integrated turbulent buoyancy flux ξ_A vs. Fr_i for spreading (open circles) and channelized (filled circles) runs. The area-integrated turbulent buoyancy flux is calculated as $\xi_A = \xi \frac{A_S}{A_C}$ in spreading runs and $\xi_A = \xi \frac{A_C}{A_C}$ in channelized runs. Linear fits in c) are applied separately for spreading (dash line) and for channelized runs (solid line). Cross symbols highlight three points (SP5, SP6, and CH1) that discussed in Figure 7.

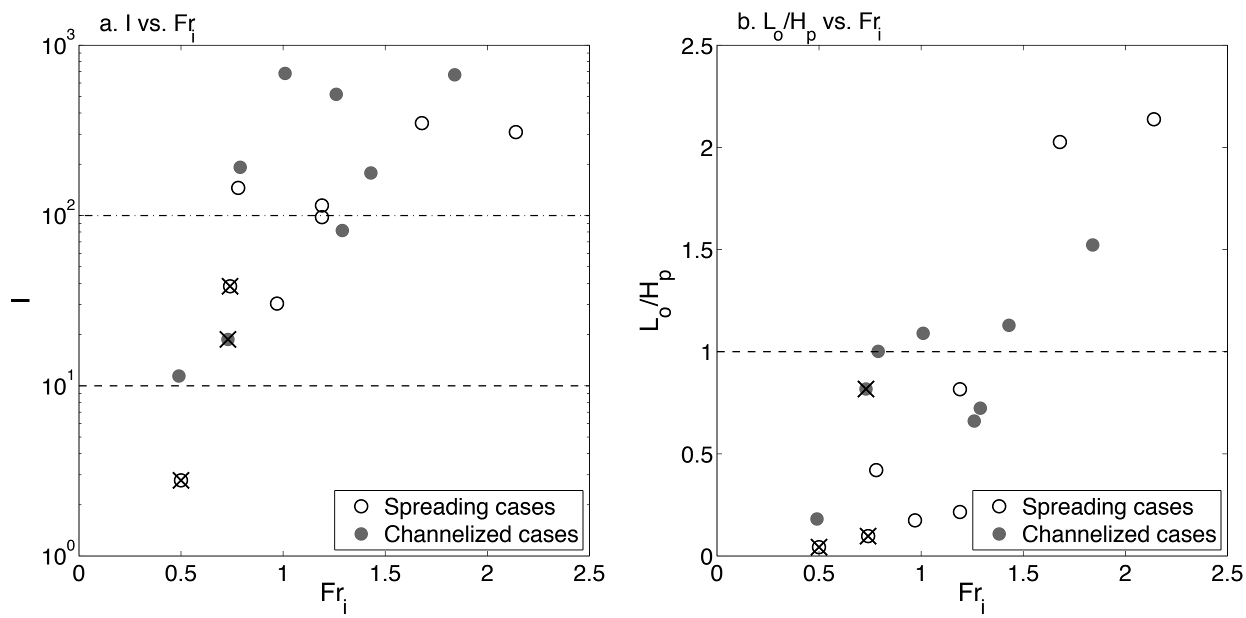

FIG. 12. a) $I = \varepsilon/\nu N^2$ vs. Fr_i, dash line and dash-dot lines are two thresholds for turbulent regime, $I = 10$ and $I = 100$. b) Ozmidov scale L_o normalized by plume thickness H_p vs. Fr_i. The dashed line is the reference for $L_o = H_p$. Cross symbols highlight three points (SP5, SP6, and CH1) that discussed in Figure 7.

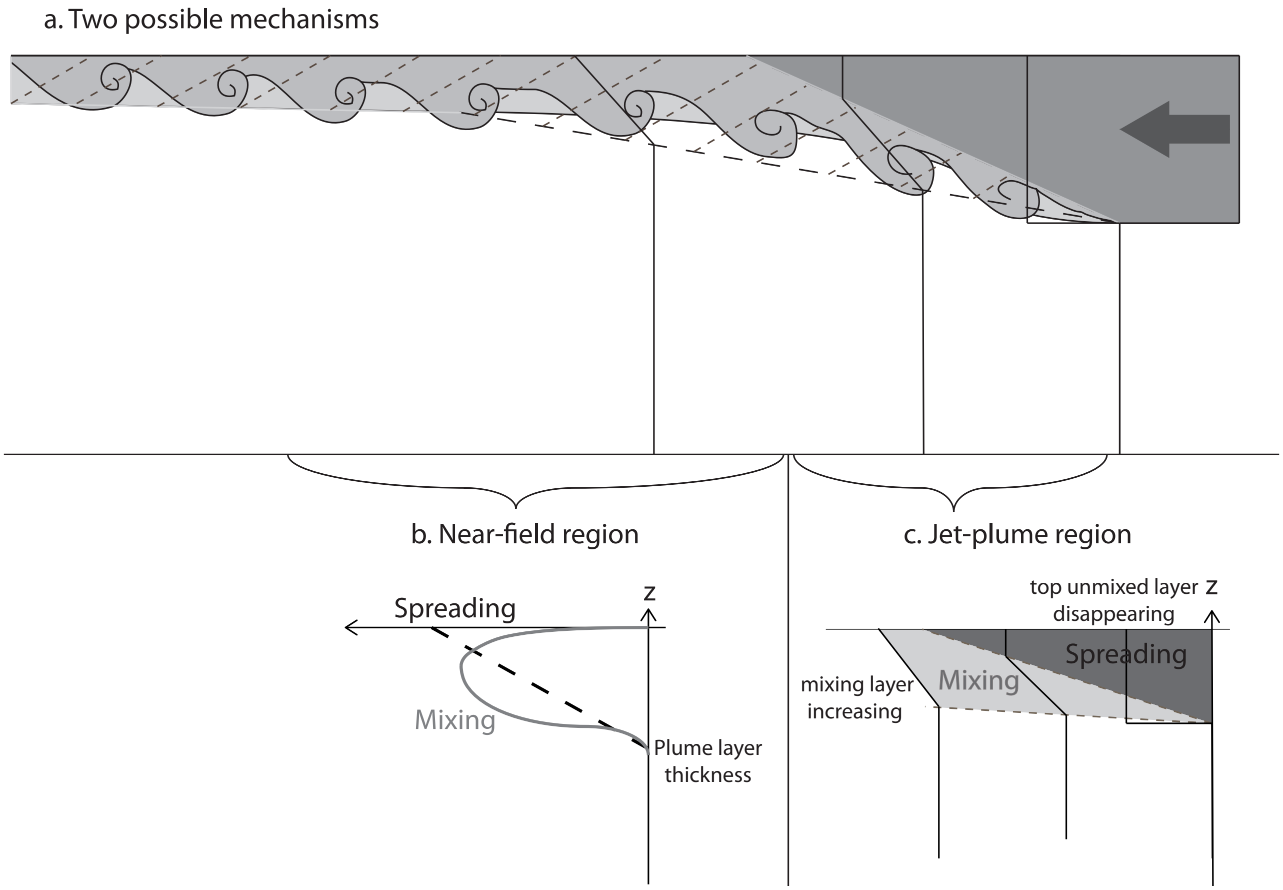

FIG. 13. Schematic representation of spreading and mixing in the jet-to-plume and near-field plume regions showing the transformation of vertical density structure (a). Three density (or velocity) profiles here represent the density profiles transforming from the fully channelized, transitional, and fully developed spreading regions, from right to left. Two possible mechanisms show the relationship between spreading and mixing in b) the near-field plume and c) the jet-plume region.

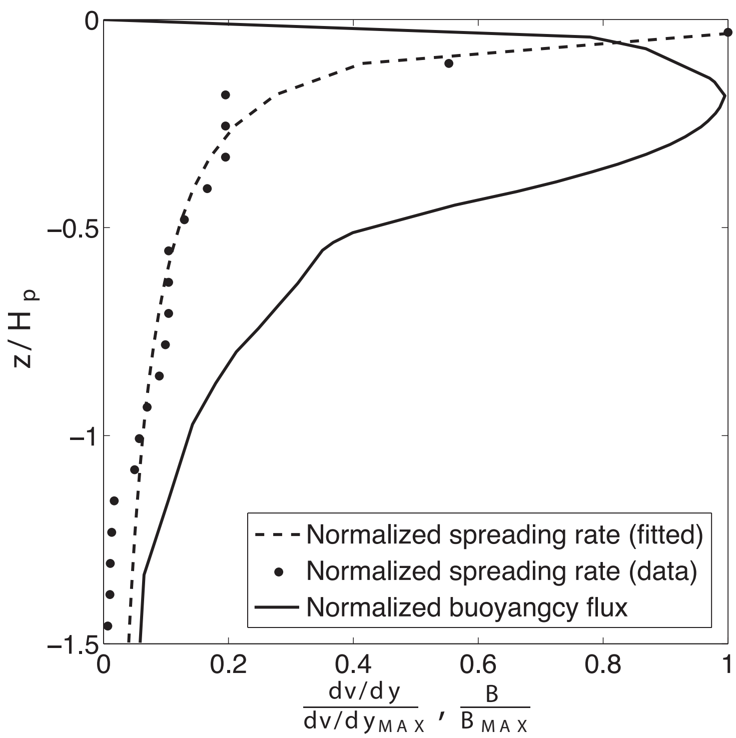

FIG. 14. Comparison of normalized spreading rate ($\frac{dv/dy}{dv/dy_{MAX}}$) profile with the normalized turbulent buoyancy flux ($\frac{B}{B_{MAX}}$) profile for an intermediate Froude number run (SP7:Fr=0.97). The dashed line is an exponential fit to the observed spreading rate profile.